Estimation and Enhancement of Tissue Motion Using Ultrasound Imaging

Md Ashikuzzaman

A Thesis
in
The Department
of
Electrical and Computer Engineering

Presented in Partial Fulfillment of the Requirements
for the Degree of
Master of Applied Science (Electrical and Computer Engineering)
Concordia University
Montreal, Quebec, Canada

August 2019

Concordia University
School of Graduate Studies

This is to certify that the thesis prepared

By: **Md Ashikuzzaman**

Entitled: **Estimation and Enhancement of Tissue Motion Using Ultrasound Imaging**

and submitted in partial fulfillment of the requirements for the degree of

Master of Applied Science

complies with the regulations of this University and meets the accepted standards with respect to originality and quality.

Signed by the final examining commitee:

Dr. Wei-Ping Zhu _____ Chair, Examiner

Dr. Thomas Fevens _____ Examiner, External To the Program

Dr. Habib Benali _____ Examiner

Dr. Hassan Rivaz _____ Supervisor

Dr. Claudine Gauthier _____ Co-supervisor

Approved by: _____

Dr. Yousef R. Shayan, Chair
Department of Electrical and Computer Engineering

August 2019 _____

Dr. Amir Asif, Dean
Gina Cody School of Engineering and Computer Science

Abstract

Estimation and Enhancement of Tissue Motion Using Ultrasound Imaging

Md Ashikuzzaman

One of the major advantages of ultrasound is its ability to image at very high frame rates, which can be exploited to track tissue motion. In this thesis, we focus on two important applications of motion estimation, namely ultrasound elastography and clutter suppression. In both of these applications, the tracking problem poses several technical challenges and as such is an active field of research. In elastography, tracking motion while a tissue undergoes some deformation reveals the physiological condition of the tissue by mapping its mechanical properties. We process ultrasound Radio-Frequency (RF) frames acquired before and after tissue deformation to estimate tissue displacement and eventually tissue strain. We propose a novel ultrasound elastography method where unlike conventional techniques, three ultrasound RF frames are taken into account to devise a cost function consisting of data term, spatial regularization terms and temporal continuity prior. We find the strain map by taking the spatial derivative of frame to frame displacement field estimated by efficient optimization of the aforementioned cost function. Validation with simulation, phantom and *in-vivo* liver data shows that the proposed technique substantially outperforms the state-of-the-art ultrasound elastography algorithms in terms of conventional quality metrics such as Signal-to-Noise Ratio (SNR), Contrast-to-Noise Ratio (CNR) and Strain Ratio (SR).

In clutter suppression, enhancement of blood flow by suppressing the clutter (i.e. non-moving stationary tissue) components is vital for assessing vascular health. In this thesis, a novel technique for suppressing clutter in ultrasound Color Flow Imaging (CFI) has also been proposed. Since the state-of-the-art Singular Value Decomposition (SVD) based technique is highly dependent on the proper selection of the boundaries between different subspaces, it is prone to producing nonoptimal clutter suppressed power Doppler images. In addition, extensive manual intervention typically needed to find the correct subspace ranks makes SVD difficult to be implemented

on clinical ultrasound machines. To overcome these limitations, we propose to look at the clutter suppression problem from the standpoint of separating the foreground from the background. Precisely, we adapt the fast Robust Matrix Completion Algorithm (fRMC) where the in-face extended Frank-Wolfe method has been taken into account to decompose the Casorati matrix into low rank clutter and sparse blood components without requiring any manual tuning. We validate the proposed algorithm with simulation, experimental flow phantom, *in-vivo* animal and human datasets to show that our technique confidently attains the optimal result without requiring any manual intervention.

Acknowledgments

First and foremost, I would like to take the opportunity to express my sincere gratitude to my great supervisors Dr. Hassan Rivaz and Dr. Claudine Gauthier without whom this work would not have been possible. I very much appreciate the technical and financial support they have provided me with. I am very thankful to them for their continuous guidance and motivation.

I would like to thank my highly capable and creative minded colleagues at IMPACT for their valuable discussions. I am very much grateful to Professor Hassan Rivaz, the director of IMPACT lab. It has been a fantastic experience to work with Professor Rivaz. When I started my MASc back in 2017, I had very little research experience. Professor Rivaz has been an excellent mentor to me, creating the initial momentum as well as guiding me towards forming a comprehensive idea about the state-of-the-art techniques of medical imaging and limitations of them. His continuous motivation and proper direction at every stage of my thesis have pushed me to accomplish apparently complicated projects. He has always been by my side whenever I went through a hard time. I cannot thank him enough for the love and affection I have received from him.

I thank Dr. Andreas Bergdahl for obtaining the ethics approval for the *in-vivo* rat experiment. I would also like to acknowledge that the rat experiment was performed under his close supervision. I am thankful to my colleagues Clyde Belasso and Md. Golam Kibria for their important collaborations in the flow phantom and *in-vivo* rat experiments respectively. I would like to thank Drs. E. Boctor, M. Choti and G. Hager for their permission to use the *in-vivo* liver data. I also thank Dr. Md Kamrul Hasan for sharing the code of the hybrid method. I would also like to acknowledge that this work has been supported in part by NSERC Discovery grant RGPIN 2015-04136 and by a New Investigator Award from the Heart and Stroke Foundation.

I would like to thank my thesis committee members Drs. Wei-Ping Zhu, Thomas Fevens, Habib Benali, Claudine Gauthier and Hassan Rivaz for their constructive

comments and invaluable suggestions for further extensions of this work.

I am grateful to my friends Asif Iqbal, Ruman Morshed, Samiul Alam, Amir Amini, Morteza Mirzaei, Sobhan Goudarzi, Jamil Reza Chowdhury, Sadeq Melhem and Siddiqur Rahman Milon (dada) for their valuable discussions and help in different stages of my study.

Finally, I thank my beloved family for their continuous support throughout my graduate studies at Concordia. I would like to express my heartiest gratitude to my father, Md Golam Kibria and mother, Salma Begum, for their sacrifice, love, constant moral support and inspiration to move forward with positive energy. I have no reservation saying that every achievement of mine has been possible because of their lifelong sacrifice and effort. I am very much grateful to my wife, Wahida Nawrin, for her love, sacrifice and continuous encouragement throughout the journey which have been vital for this accomplishment. I would like to thank my brother, Md Hadiuzzaman and sister, Sharmin Sultana, for always believing in my abilities and taking good care of my parents over there in Bangladesh. I am also very thankful to my sister-in-law, Tonni Zaman and brother-in-law, Mahbub Haq, for their good wishes. I want to express my heartfelt affection for my nephew, Ahnaf Haq and niece, Zahabia Tasnim (Toru) who have always been sources of my pleasure.

Contents

List of Figures

List of Tables

Chapter 1

Introduction

1.1 Basics of Ultrasound Imaging

Ultrasonic imaging is one of the most widely used medical imaging modalities which operates using the transmission and reflection of high frequency sound wave. Although acoustic waves which have frequencies higher than 20 kHz are considered to be ultrasound, medical ultrasound systems utilize sound waves of the frequency range 1-20 MHz. Ultrasound has gained popularity due to its non-invasive, cost-effective and easy-to-use nature. In addition, numerous applications such as determining the gender, position and overall condition of the fetus, diagnosing the physiological condition of the tissue and vasculature, detection of kidney stones and prostate cancer etc. have made ultrasound attractive for wide clinical adoption.

The probe is a very important component of an ultrasound system. It consists of a series of piezoelectric crystals called transducers which are responsible for generating and transmitting the sound pulse using the piezoelectric effect. Once the crystals are electrically excited, they immediately change shape or start to vibrate. This vibration produces acoustic signal and this signal is transmitted outward. When the probe is attached to the body, sound wave generated from the transducers travel through the tissue. Whenever this travelling longitudinal acoustic wave encounters a boundary between two different types of tissue, a portion of it reflects back to the probe. The amount of sound wave reflected back to the probe depends on the reflectivity of the tissue. The remaining portion of the wave keeps propagating through the tissue until it finds another tissue boundary. The portion of the sound wave which gets back to the probe is received by the same piezoelectric crystals which generated the waves. This

reflected sound wave is then converted back to the electrical signal by the transducers. This raw signal is known as Radio-Frequency (RF) or unprocessed ultrasound signal. RF data is processed in several steps before being displayed on the screen of the ultrasound machine. Logarithmic (log) compression of the envelope of the RF data is performed internally and a two dimensional Brightness image (B-mode) is formed. This B-mode image is shown on the screen of the ultrasound machine. A more comprehensive overview of ultrasound imaging can be found in [1–3]. Figure 1.1 shows the picture of the Alpinion E-Cube R12 research ultrasound system at the PERFORM centre of Concordia University.

Depending on the arrangement of the piezoelectric crystals, probes are mainly divided into two classes: linear array and curvilinear. As the name suggests, the transducers are organized along a line in case of a linear array probe. Usually, linear array probes utilize high frequency ultrasound waves. Since high frequency waves attenuate very fast, linear array probes are used to image the structures at shallow depth. The main advantage of using a linear array probe is that it can acquire images at high spatial resolution. In contrast to linear array probes, curvilinear probes are used to image deeper structures such as abdomen since they deal with low frequency waves. Although curvilinear ultrasound probes are capable of collecting images with a wide field of view, they suffer from lower resolution. Figure 1.2 shows the pictures of linear array and curvilinear probes. The aforesaid two types of probes do not work for organs which are only observable from a small acoustical window because of their large footprint. For instance, it is very difficult to perform cardiac or transcranial imaging with linear or curvilinear ultrasound probes. Having a small footprint, a phased array probe resolves this issue by imaging through small acoustic window with wide field of view and low frequency. A depiction of linear, curvilinear and phased-array ultrasound probes is provided in Figure 1.3. In addition, some probes are specially designed to be able to get closer to the target organ through different openings of the body. Furthermore, $3D$ ultrasound image can be collected by using a probe containing a $2D$ array of transducers. More details about ultrasound probes can be found in [4].

Figure 1.1: Alpinion E-Cube R12 research ultrasound machine at PERFORM centre, Concordia University.

(a) Linear array probe (b) Curvilinear probe

Figure 1.2: Different types of ultrasound probes. The left and right figures show linear array and curvilinear probes respectively.

Figure 1.3: From left to right: linear, curvilinear and phased-array ultrasound probes and images collected by them. Picture courtesy of Luca et al., 2018.

1.2 Motion Tracking and Enhancement Using Ultrasound

Over the last few decades, tracking and enhancing the tissue motion using ultrasound have facilitated the diagnosis of different disease states. Ultrasound elastography is a promising technique to track tissue motion for detecting the physiological condition of the tissue undergoing deformation. On the other hand, enhancing the blood flow by suppressing the clutter components of ultrasound color flow images have been successful in characterizing the vasculature. We provide a brief overview of these two different fields below.

1.2.1 Ultrasound Elastography

Ultrasound elastography is a non-invasive method to infer the elasticity of a tissue under consideration. Elastography has become increasingly popular in disease diagnosis, image-guided surgery and many other clinical interventions. Ultrasound elastography has been successful in diagnosing cyst in the liver [5, 6], solid and fluid filled breast lesions [7]. Since the malignant cells are prone to be harder than the normal cells [8], tissue elasticity mapping is a promising tool for classifying malignancy. Ultrasound elastography can be categorized into several classes: dynamic [9], quasi-static [5–7], Acoustic Radiation Force Impulse Imaging (ARFI) [10] etc. This thesis focuses on quasi-static elastography technique. Two ultrasound RF frames are taken into consideration in quasi-static ultrasound elastography: one before and another after the tissue deformation. The displacement field between these two frames are calculated using a speckle tracking algorithm. Spatial differentiation of this displacement field is performed to obtain the strain map which is capable of distinguishing the pathological tissue from the normal one. A schematic depiction of the steps involved in quasi-static ultrasound elastography is presented in Figure 1.4.

1.2.2 Ultrasound Clutter Suppression

Suppressing clutter components in ultrasound Color Flow Imaging (CFI) is necessary to ensure a clear visualization of the vascular network. An unambiguous view of the vascular structure is important to assess diabetes and its related diseases, ischemia, aneurysm and coronary heart diseases [11–14]. Blood exhibits a different frequency

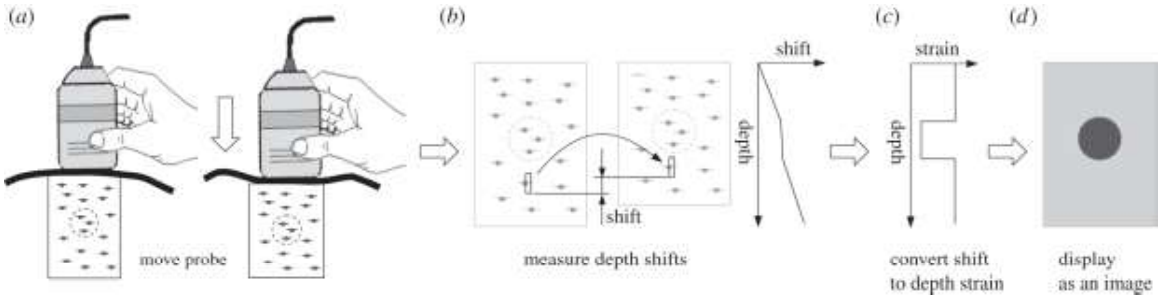

Figure 1.4: Schematic depiction of quasi-static ultrasound elastography. Courtesy: Treece et al., *Interface Focus*, 2011.

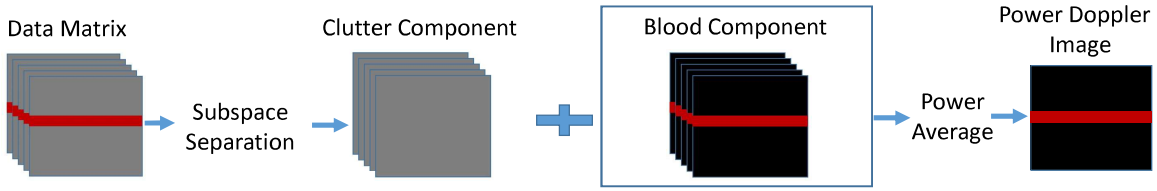

Figure 1.5: Schematic presentation of ultrasound clutter suppression.

spectrum than normal tissue since it has higher velocity. A difference in strength of backscattered signal is another important factor behind the frequency spectra being different. This difference in frequency components was initially exploited to reject clutter by high pass filtering [15, 16]. However, high pass filtering fails to find the correct boundary between the frequency components corresponding to blood and clutter in cases of dominant tissue motion or unintentional hand motion of the sonographer since the frequency spectra overlaps with each other. To mitigate this drawback, eigen based clutter filtering methods have been proposed [17–23]. In these techniques, the blood subspace is separated from the clutter based on the eigen components of the data matrix (see Figure 1.5). Although these methods are capable of distinguishing blood from clutter adaptively, extensive manual tuning is needed to find the proper boundary between blood and clutter subspaces.

1.3 Objectives of the Thesis

This objective of this thesis is to exploit the high frame-rate of ultrasound to enhance its capabilities. To that end, we focus on two active fields of research, namely elastography and clutter suppression. First, we propose a novel ultrasound elastography algorithm that unlike conventional methods, utilizes three ultrasound RF frames in a

novel cost function. This cost function consists of echo intensity similarity terms, spatial continuity terms and temporal regularization terms. This non-linear cost function has been optimized efficiently and a sparse system of equations has been formulated to solve for millions of variables for obtaining the frame to frame displacement fields. Adaptive spatial regularization has been taken into account to amend the possible underestimation of the displacement. In addition, an adaptive temporal continuity term is introduced to handle the instances of temporal decorrelation. The parameters of the technique have been tuned carefully to obtain the optimal result for the displacement map. Finally, the displacement field has been differentiated spatially to find the strain image. The method has been validated with simulation data containing a soft inclusion. Different levels of noise has been added to the simulation data to show the robustness of the proposed method to noise. In addition to simulation, results have been reported for experimental breast phantom. Finally, the *in-vivo* (data collected from a living organism) feasibility of the technique has been demonstrated by validating against three sets of liver cancer data.

Second, we develop a novel technique to suppress clutter components in ultrasound color flow imaging. The primary goal of this method is to facilitate clutter rejection without requiring any manual tuning. The clutter suppression problem has been solved by modelling the steady clutter and blood as low rank and sparse components respectively. Specifically, an optimization problem formulated with the fast Robust Matrix Completion (fRMC) algorithm [24] has been solved by in-face extended Frank-Wolfe algorithm [25] to extract the sparse blood component from the spatio-temporal data matrix. This method requires no manual intervention and is capable of obtaining clutter suppressed power Doppler images as good as the conventional Singular Value Decomposition (SVD) and Principal Component Analysis (PCA) based techniques. Validation with simulation, phantom, *in-vivo* animal and human datasets proves the viability of the proposed method. Extensive quantitative and statistical analysis have been performed to validate the method and compare it to previous work.

1.4 Organization of the Thesis

This thesis has been outlined as follows. In Chapter 2, a novel real time quasi-static ultrasound elastography algorithm GUEST: **G**lobal **U**ltrasound **E**lastography in **S**patial and **T**emporal Domains [26] has been presented. Chapter 3 describes RAPID: **R**obust m**A**trix decom**P**osition for suppress**I**ng clutter in ultrasoun**D** [27],

a novel algorithm for ultrasound clutter rejection. This work is an extension of [28]. Chapter 4 wraps up the thesis with possible future work and concluding remarks. In Appendices A and B, additional results and analyses have been presented for Chapter 2 and Chapter 3 respectively.

1.5 Publications

This thesis has culminated in the following publications:

- M. Ashikuzzaman, C. J. Gauthier, and H. Rivaz, "Global Ultrasound Elastography in Spatial and Temporal Domains", *IEEE Transactions on Ultrasonics, Ferroelectrics and Frequency Control (TUFFC)*, vol. 66, no. 5, pp. 876-887, 2019.

- M. Ashikuzzaman, C. Belasso, C. J. Gauthier, and H. Rivaz, "Suppressing clutter components in ultrasound color flow imaging using robust matrix completion algorithm: Simulation and phantom study", in *IEEE International Symposium on Biomedical Imaging (IEEE ISBI)*, Venice, Italy, 2019.

- M. Ashikuzzaman, C. J. Gauthier, and H. Rivaz, "Temporally Regularized Global Ultrasound Elastography", *16th International Tissue Elasticity Conference (ITEC)*, Avignon, France, 2018 **(Selected as a finalist for the best student paper award)**.

- M. Ashikuzzaman, C. Belasso, M. G. Kibria, A. Bergdahl, C. J. Gauthier and H. Rivaz, "Low Rank and Sparse Decomposition of Ultrasound Color Flow Images for Suppressing Clutter in Real Time", *IEEE Transactions on Medical Imaging (TMI)*, revision under review, 2019.

Chapter 2

Global Ultrasound Elastography in Spatial and Temporal Domains

In this chapter, a novel computationally efficient quasi-static ultrasound elastography technique is introduced by optimizing an energy function. Unlike conventional elastography techniques, three Radio-Frequency (RF) frames are considered to devise a non-linear cost function consisting of a data-intensity similarity term, spatial regularization terms and most importantly, temporal continuity terms. We optimize the aforesaid cost function efficiently to obtain Time Delay Estimation (TDE) of all samples between the first two and last two frames of ultrasound images simultaneously, and spatially differentiate the TDE to generate axial strain map. A novelty in our spatial and temporal regularizations is that they adaptively change based on the data, which leads to substantial improvements in TDE. We handle the computational complexity resulting from incorporation of all samples from all three frames by converting our optimization problem to a sparse linear system of equations. Consideration of both spatial and temporal continuity makes the algorithm more robust to signal decorrelation than the previous algorithms. We name the proposed method GUEST: Global Ultrasound Elastography in Spatial and Temporal directions. We validated our technique with simulation, experimental phantom and *in-vivo* liver data and compare the results with two recently proposed TDE methods. In all experiments, GUEST substantially outperforms other techniques in terms of Signal to Noise Ratio (SNR), Contrast to Noise Ratio (CNR) and Strain Ratio (SR) of the strain images.

2.1 Introduction

Ultrasound Elastography is a non-invasive medical imaging technique to infer mechanical properties of tissue by utilizing ultrasound Radio-Frequency (RF) data. Elastography is increasingly being applied in diagnosis, image-guided surgery and numerous other clinical applications [29, 30]. Among several types of clinically adopted elastography techniques, it can broadly be classified into two classes: "dynamic" which involves constant monitoring of tissue response to time-varying forces to quantify the mechanical properties of the tissue, and "quasi-static" which estimates slow deformation of tissue due to an approximately constant force [31–34]. Within the broad class of quasi-static elastography, our work is based on free-hand palpation elastography. Free-hand palpation elastography often suffers from decorrelation between pre- and post-compression images due to out-of-plane motion of the probe, blood flow in vessels, incoherent motion of fluid in fluid-filled lesions and the 3D nature of tissue deformation even with purely an axial probe motion [5]. Despite these drawbacks, this method has generated interest due to its ease-of-use, since free-hand palpation elastography involves holding the probe and pressing the region of interest without requiring any additional tool [35–39].

Time Delay Estimation (TDE) is a necessary step in all ultrasound elastography methods. Unfortunately, TDE is an ill-posed problem because one sample of RF data by itself does not provide enough information for tracking. Therefore, two distinct classes of methods have emerged to solve this problem. In the first class, RF data is divided into several windows and it is assumed that the displacements of all samples in a particular window are same. The additional samples in the window provide enough information for tracking [7, 40–43]. The second class penalizes displacement discontinuity between neighboring samples and calculates a displacement estimate for all samples of RF data. These methods are named regularized optimization-based or energy-based techniques [5, 6, 44–47]. The windowing in the first class and discontinuity penalty in the second class can be considered as hard and soft regularization respectively. Between the two aforementioned techniques, window-based or block matching algorithms are more commonly used. In window-based techniques, RF data is divided into several blocks and displacement of each block is found either by looking at the maximum cross correlation [32, 48–51] or zero phase crossing [43, 52, 53]. Block matching algorithms make an inherent compromise between spatial resolution

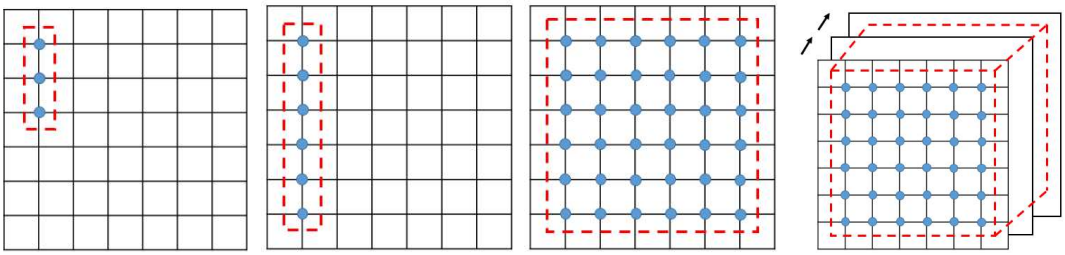

(a) window-based (b) DPAM (c) GLUE (d) GUEST

Figure 2.1: Estimation of displacement field in window-based, DPAM, GLUE and GUEST algorithms. Blue dots represent samples of RF data used in displacement estimation, and the dashed window shows how the data is divided to estimate displacement fields. In (a), the data in the window is used to estimate the displacement of the central sample. In (b) and (c), displacement of all samples in an RF-line and the entire image are used, respectively, to estimate the displacement field of all these samples simultaneously. In (d), three RF frames are considered and both spatial and temporal continuity constraints are enforced. Displacement of all samples in these frames are calculated simultaneously.

and accuracy based on the size of window. On the one hand, a more accurate displacement field can be obtained if the window size is ten times the ultrasound wavelength or even larger [54]. The accuracy is higher because a large correlation window reduces the estimation variance, also known as jitter error [51,55]. Since the RF signal is non-stationary, a large window induces signal decorrelation [51, 56] and hence amplifies noise. On the other hand, better spatial resolution can be achieved by sacrificing accuracy and selecting smaller windows. The displacement estimation can be performed in either the axial direction [32, 57, 58] or both axial and lateral directions [59–61]. The downside of the two-dimensional search is that it is computationally more expensive. In addition, the lateral displacement field is substantially less accurate than the axial displacement field due to the low resolution of ultrasound in this direction.

TDE techniques that are based on minimization of cost functions are robust to signal decorrelation as the displacement continuity assumption is exploited to reduce estimation variance. The drawback of optimization based techniques lies in the fact that these techniques are hard to implement in real-time due to their computational complexity [45, 62]. This problem can be alleviated by using Dynamic Programming (DP) [44] which efficiently calculates the integer displacement field between two RF frames. However, integer displacement field alone does not suffice for the accurate and smooth TDE requirement. Efficient minimization of a cost function involving data and displacement continuity terms to calculate the subsample displacement field was

introduced in Dynamic Programming Analytic Minimization (DPAM) [5]. DPAM takes the initial integer displacement field from DP [44], and calculates the subsample axial and lateral displacements of all samples of one column of RF data. Since each column of RF data is optimized independently, discontinuity between the RF lines leads to some vertical stripes in the TDE. GLobal Ultrasound Elastography (GLUE) [6] resolved this drawback by considering the whole image for calculating the subsample displacement field. It is worth mentioning that, like DPAM, GLUE takes the initial displacement field from DP.

Though the displacement field estimated by GLUE is spatially accurate and smooth, information in the temporal domain still remains unexploited. In this chapter, we introduce a novel technique called Global Ultrasound Elastography in Spatial and Temporal directions (GUEST) where three consecutive RF frames are incorporated instead of two to estimate the axial and lateral displacement fields. We utilize information in 3 frames, and enforce temporal continuity constraints on the displacement field to *simultaneously* estimate two 2D displacement fields. In other words, assuming that the 3 frames are I_1, I_2 and I_3, and the 2D displacement fields between I_1 and I_2 is d^1, and between I_2 and I_3 is d^2, we impose temporal constraints on d^1 and d^2. Window-based methods, DPAM, GLUE and GUEST can be summarized as follows (see also Figure 2.1):

- **Window-based methods**: The displacement of each window (few ultrasound wavelengths) is calculated together.
- **DPAM**: Displacements of all samples of a single RF line are calculated together. Axial continuity is utilized to reduce estimation variance.
- **GLUE**: Displacements of all samples of a single image are calculated together. Axial and lateral continuities are utilized to reduce estimation variance.
- **GUEST**: The displacement of all samples of multiple images is calculated together. Axial, lateral and temporal continuities are utilized to reduce estimation variance.

In addition to utilizing multiple images, another contribution of this work is the introduction of adaptive regularization terms. Instead of assuming equal displacements in the spatial domain or constant velocity in the temporal domain, we propose data-driven spatial and temporal regularization terms. Exploiting multiple images

and using adaptive regularization terms leads to substantial improvements in the quality of the strain images in GUEST compared to GLUE. Specifically, adaptive spatial regularization prevents underestimation of the displacement field. Adaptive temporal regularization accounts for variations in probe velocity, which leads to different strain levels between consecutive frames. We describe these two regularization terms in the Methods Section.

TDE using three images has been considered before [47]. However, there are two major differences. First, TDE optimization was limited to single RF lines like DPAM. Second, a linear stress-strain relationship was assumed, which may not always hold. GUEST is validated using simulation, phantom and *in-vivo* data, and is compared to recent window-based and optimization-based methods [6, 7]. GUEST substantially outperforms both methods in all experiments. An implementation of GUEST can be found at `https://users.encs.concordia.ca/~hrivaz/Ultrasound_Elastography/`.

2.2 Methods

Assume I_1 and I_2 are two RF frames of size $m \times n$ collected from a tissue before and after deformation respectively. Our aim is to calculate the axial and lateral displacement fields a and l which accurately map the pre-compression image I_1 to the post-compression image I_2. After finding the displacement fields, it is common to spatially differentiate them to obtain strain images. We first briefly explain GLUE [6], a closely related previous technique which calculates a and l. We then present GUEST and derive the mathematical equations to calculate displacement fields while enforcing spatio-temporal continuity constraints.

2.2.1 Global Time Delay Estimation (GLUE)

GLUE uses DP [44], an efficient non-iterative method for global optimization, to get initial time delay estimations in axial ($a_{i,j}$) and lateral ($l_{i,j}$) directions, where $1 \leq i \leq m$ and $1 \leq j \leq n$ denote the location in the image. DP alone provides integer displacement estimates, which is not enough to provide an accurate displacement estimation. To this end, GLUE adds subsample estimation $\Delta a(i,j)$ and $\Delta l(i,j)$ to DP displacements. $\Delta a(i,j)$ and $\Delta l(i,j)$ are obtained from the minimization of the following regularized cost function:

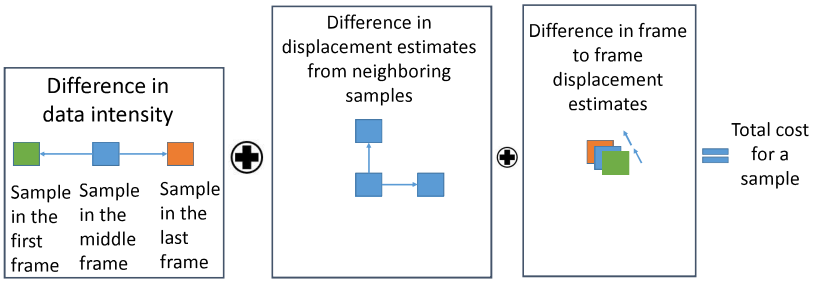

Figure 2.2: An illustration of the cost function.

$$
\begin{aligned}
&C(\Delta a_{1,1}, ..., \Delta a_{m,n}, \Delta l_{1,1}, ..., \Delta l_{m,n}) = \\
&\sum_{j=1}^{n}\sum_{i=1}^{m}\{[I_1(i,j) - I_2(i + a_{i,j} + \Delta a_{i,j}, j + l_{i,j} + \Delta l_{i,j})]^2 \\
&+ \alpha_1(a_{i,j} + \Delta a_{i,j} - a_{i-1,j} - \Delta a_{i-1,j})^2 \\
&+ \alpha_2(a_{i,j} + \Delta a_{i,j} - a_{i,j-1} - \Delta a_{i,j-1})^2 \\
&+ \beta_1(l_{i,j} + \Delta l_{i,j} - l_{i-1,j} - \Delta l_{i-1,j})^2 \\
&+ \beta_2(l_{i,j} + \Delta l_{i,j} - l_{i,j-1} - \Delta l_{i,j-1})^2\}
\end{aligned}
\tag{1}
$$

where α_1 and α_2 are regularization parameters for axial displacements, and β_1 and β_2 are regularization parameters for lateral displacements. By minimizing this cost function, GLUE converts the optimization problem into a linear set of equations of the classical form $Ax = b$. By solving the aforemention linear set of equations, GLUE finds the subsample displacement field and adds it to the initial estimate to obtain total displacement field.

2.2.2 GUEST: Global Ultrasound Elastography, Spatio-Temporal

We utilize three frames during tissue compression, and enforce adaptive spatial and temporal priors on the displacement field. This is in contrast to GLUE, which only considers spatial priors, and further does not adapt the priors to better represent the data. Let I_1, I_2 and I_3 be three RF frames, and a^1, l^1, a^2 and l^2 be axial and lateral DP integer displacement estimates from frame 1 to frame 2, and from frame 2 to frame 3 respectively.

GUEST simultaneously estimates refinements Δa^1, Δl^1, Δa^2 and Δl^2 and adds them to integer DP displacement fields. To that end, we construct a cost function

Table 2.1: Definition of the variables, parameters, vectors and matrices

Notation	Definition
I_1, I_2, I_3	RF frames
$a^1_{i,j}$, $a^2_{i,j}$	Axial displacement estimates from DP
$l^1_{i,j}$, $l^2_{i,j}$	Lateral displacement estimates from DP
$\Delta a^1_{i,j}$, $\Delta a^2_{i,j}$	Subsample axial displacements from GUEST
$\Delta l^1_{i,j}$, $\Delta l^2_{i,j}$	Subsample Lateral displacements from GUEST
D_g	Data intensity similarity term
R_s	Spatial continuity term
R_t	Temporal continuity term
α_1, α_2	Axial regularization parameters
β_1, β_2	Lateral regularization parameters
α_3, β_3	Temporal regularization parameters
ϵ^k_a, ϵ^k_l	Adaptive spatial regularization parameters
γ_a, γ_l	Adaptive temporal regularization parameters
D	Matrix containing regularization parameters
H, H_1	Matrices containing data derivatives
μ	Vector containing data differences
d	Vector containing TDEs from DP
Δd	Vector containing subsample TDEs
b_t	Adaptive temporal continuity vector
b_s	Adaptive spatial continuity vector

including data terms, spatial continuity terms and temporal continuity terms as follows (see also Figure 2.2):

$$\begin{aligned} &C(\Delta a^1_{1,1}, \Delta l^1_{1,1}, ..., \Delta a^1_{m,n}, \Delta l^1_{m,n}, \Delta a^2_{1,1}, \Delta l^2_{1,1}, ..., \Delta a^2_{m,n}, \\ &\Delta l^2_{m,n}) = \sum_{j=1}^{n} \sum_{i=1}^{m} \{D_g + R_s + R_t\} \end{aligned} \tag{2}$$

Here, D_g stands for data of the GUEST method and is defined as follows:

$$\begin{aligned} D_g &= [I_2(i,j) - I_1(i - a^1_{i,j} - \Delta a^1_{i,j}, j - l^1_{i,j} - \Delta l^1_{i,j})]^2 \\ &+ [I_2(i,j) - I_3(i + a^2_{i,j} + \Delta a^2_{i,j}, j + l^2_{i,j} + \Delta l^2_{i,j})]^2 \end{aligned} \tag{3}$$

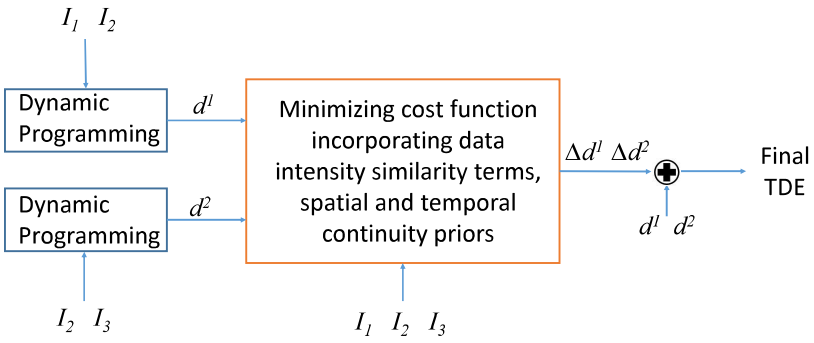

Figure 2.3: Flow diagram demonstration of the proposed GUEST algorithm.

R_s and R_t are adaptive spatial and temporal regularization terms respectively and are elaborated below.

Adaptive Spatial and Temporal Regularizations

Spatial regularization terms considered in GLUE assumed that displacement of a sample should ideally be the same as the displacement of neighbouring sample. However, this assumption is not necessarily correct in elastography. Often, such constraint results in the underestimation of the displacement field [5]. To compensate for the anticipated underestimation, we introduce adaptive spatial regularization terms of the form $\alpha(disp_i - disp_{i-1} - \epsilon)^2$ instead of $\alpha(disp_i - disp_{i-1})^2$, where ϵ is the average difference between the displacement of two neighboring pixels i and $i-1$. As such, the spatial regularization R_s is defined as follows:

$$
\begin{aligned}
R_s = {} & \alpha_1(a^1_{i,j} + \Delta a^1_{i,j} - a^1_{i-1,j} - \Delta a^1_{i-1,j} - \epsilon^1_a)^2 \\
& + \alpha_1(a^2_{i,j} + \Delta a^2_{i,j} - a^2_{i-1,j} - \Delta a^2_{i-1,j} - \epsilon^2_a)^2 \\
& + \alpha_2(a^1_{i,j} + \Delta a^1_{i,j} - a^1_{i,j-1} - \Delta a^1_{i,j-1} - \epsilon^1_a)^2 \\
& + \alpha_2(a^2_{i,j} + \Delta a^2_{i,j} - a^2_{i,j-1} - \Delta a^2_{i,j-1} - \epsilon^2_a)^2 \\
& + \beta_1(l^1_{i,j} + \Delta l^1_{i,j} - l^1_{i-1,j} - \Delta l^1_{i-1,j} - \epsilon^1_l)^2 \\
& + \beta_1(l^2_{i,j} + \Delta l^2_{i,j} - l^2_{i-1,j} - \Delta l^2_{i-1,j} - \epsilon^2_l)^2 \\
& + \beta_2(l^1_{i,j} + \Delta l^1_{i,j} - l^1_{i,j-1} - \Delta l^1_{i,j-1} - \epsilon^1_l)^2 \\
& + \beta_2(l^2_{i,j} + \Delta l^2_{i,j} - l^2_{i,j-1} - \Delta l^2_{i,j-1} - \epsilon^2_l)^2
\end{aligned}
\tag{4}
$$

where α_1, α_2, β_1, β_2 are axial and lateral regularization weights respectively. ϵ^k_a and ϵ^k_l are axial and lateral offset terms respectively that adaptively change based on the level of strain. The superscript k is 1 when comparing I_1 to I_2, and is 2 when

comparing I_2 to I_3. They are average difference in axial and lateral displacements between two neighboring samples and are calculated as follows:

$$\epsilon_a^k = \frac{a_m^k - a_1^k}{m-1}, \quad \epsilon_l^k = \frac{l_n^k - l_1^k}{l-1} \tag{5}$$

Before introducing the temporal regularization, it is useful to revisit some basic physics concepts. Both a and l are displacements with a unit such as mm. However, the ultrasound frame rate usually does not change during a single data collection and therefore a and l can also be considered velocity with a unit such as mm/T, where T is the time interval between two frames. Now $a^2 - a^1$ is the changes in velocity and therefore can be considered as acceleration with a unit such as mm/T^2. In free hand palpation elastography, it is unlikely that velocity of the probe is constant. Therefore, we introduce an adaptive temporal regularization that takes into account non-zero accelerations. As such, R_l is defined as:

$$\begin{aligned} R_t = \alpha_3 (a_{i,j}^2 + \Delta a_{i,j}^2 - a_{i,j}^1 - \Delta a_{i,j}^1 - \gamma_a)^2 \\ + \beta_3 (l_{i,j}^2 + \Delta l_{i,j}^2 - l_{i,j}^1 - \Delta l_{i,j}^1 - \gamma_l)^2 \end{aligned} \tag{6}$$

where, α_3 and β_3 denote temporal regularization weights in the axial and lateral directions respectively. Intuitively, instead of penalizing $a^2 - a^1$ or $l^2 - l^1$, the γ terms allow them to be different without any penalty. γ_a and γ_l approximate axial and lateral accelerations respectively and are defined as follows:

$$\gamma_a = \frac{\sum_{j=1}^{n}\sum_{i=1}^{m}\{K_g * a_{i,j}^2 - K_g * a_{i,j}^1\}}{mn}, \; \gamma_l = \frac{\sum_{j=1}^{n}\sum_{i=1}^{m}\{K_g * l_{i,j}^2 - K_g * l_{i,j}^1\}}{mn} \tag{7}$$

where K_g is a Gaussian kernel, which is used to average displacement estimates to obtain an estimate of acceleration with small variance.

Optimization of the Cost Function

R_s and R_t in (2) are quadratic in the unknowns, but the data term D_g is highly nonlinear since all the unknowns appear inside the nonlinear "functions" I_1, I_2 and I_3. Our goal is now to simplify this nonlinear function into a quadratic function by using $2D$ Taylor series expansion of the data term as follows:

$$D_g \approx \sum_{j=1}^{n}\sum_{i=1}^{m}\{[I_2(i,j) - I_1(i - a^1_{i,j}, j - l^1_{i,j}) + \Delta a^1_{i,j} I^{'}_{1,a} + \Delta l^1_{i,j} I^{'}_{1,l}]^2 + [I_2(i,j) - I_3(i + a^2_{i,j}, j + l^2_{i,j}) - \Delta a^2_{i,j} I^{'}_{3,a} - \Delta l^2_{i,j} I^{'}_{3,l}]^2\} \quad (8)$$

This equation is now quadratic in unknowns, and therefore, the cost function of Eq. 2 can be optimized by setting the partial derivatives with respect to unknowns to zero. Namely, we set $\frac{\partial C_{i,j}}{\partial \Delta a^1_{i,j}} = 0$, $\frac{\partial C_{i,j}}{\partial \Delta l^1_{i,j}} = 0$, $\frac{\partial C_{i,j}}{\partial \Delta a^2_{i,j}} = 0$ and $\frac{\partial C_{i,j}}{\partial \Delta l^2_{i,j}} = 0$ for $i = 1, 2, 3, ..., m$ and $j = 1, 2, 3, ..., n$. We organize unknown subsample displacements of $2mn$ samples in $\Delta d = [\Delta a^1_{1,1}, \Delta l^1_{1,1}, \ldots, \Delta a^1_{m,n}, \Delta l^1_{m,n}, \Delta a^2_{1,1}, \Delta l^2_{1,1}, \ldots, \Delta a^2_{m,n}, \Delta l^2_{m,n}]^T$ and the known initial estimates in $d = [a^1_{1,1}, l^1_{1,1}, \ldots, a^1_{m,n}, l^1_{m,n}, a^2_{1,1}, l^2_{1,1}, \ldots, a^2_{m,n}, l^2_{m,n}]^T$. After some algebraic operations, we get:

$$(H + D)\Delta d = H_1 \mu - Dd + b_t + b_s \quad (9)$$

$H = diag(F_1, F_3)$ is a symmetric tridiagonal matrix where $F_t = diag(h_t^{'2}(1,1), h_t^{'2}(1,2), .., h_t^{'2}(m,n))$. Here, $t \in \{1, 3\}$. The entries of F_t are defined by:

$$h_t^{'2}(i,j) = \begin{bmatrix} I^{'}_{t,a}{}^2(i,j) & I^{'}_{t,a}(i,j) I^{'}_{t,l}(i,j) \\ I^{'}_{t,a}(i,j) I^{'}_{t,l}(i,j) & I^{'}_{t,l}{}^2(i,j) \end{bmatrix} \quad (10)$$

where $I^{'}_{t,a}(i,j)$ and $I^{'}_{t,l}(i,j)$ denote the derivatives of I_t in the axial and lateral directions at the point $(i + a_{i,j}, j + l_{i,j})$.

$H_1 = diag(F^{'}_1, F^{'}_3)$ is a diagonal matrix where $F^{'}_t = diag(I^{'}_{t,a}(1,1), I^{'}_{t,l}(1,1), I^{'}_{t,a}(1,2), I^{'}_{t,l}(1,2), ..., I^{'}_{t,a}(m,n), I^{'}_{t,l}(m,n))$ and

$$\mu = \begin{bmatrix} g_1 & g_2 \end{bmatrix}^T \quad (11)$$

where

$$g_1 = \begin{bmatrix} I_2^{1,1} - I_1^{1-a^1_{1,1}, 1-l^1_{1,1}} & \ldots & I_2^{m,n} - I_1^{m-a^1_{m,n}, n-l^1_{m,n}} \end{bmatrix} \quad (12)$$

$$Q^{'} = \begin{bmatrix} \alpha_1+\alpha_2+\alpha_3 & 0 & -\alpha_2 & 0 & 0 & \dots & \dots & 0 \\ 0 & \beta_1+\beta_2+\beta_3 & 0 & -\beta_2 & 0 & \dots & \dots & 0 \\ -\alpha_2 & 0 & \alpha_1+2\alpha_2+\alpha_3 & 0 & -\alpha_2 & \ddots & \ddots & 0 \\ 0 & -\beta_2 & 0 & \beta_1+2\beta_2+\beta_3 & 0 & -\beta_2 & \ddots & 0 \\ \vdots & \ddots & \ddots & \ddots & \ddots & \ddots & \ddots & \vdots \\ \vdots & \ddots & \ddots & \ddots & \ddots & \ddots & \ddots & -\beta_2 \\ \vdots & \ddots & \ddots & \ddots & -\alpha_2 & 0 & \alpha_1+\alpha_2+\alpha_3 & 0 \\ 0 & \dots & \dots & \dots & 0 & -\beta_2 & 0 & \beta_1+\beta_2+\beta_3 \end{bmatrix} \tag{13}$$

$$R^{'} = \begin{bmatrix} 2\alpha_1+\alpha_2+\alpha_3 & 0 & -\alpha_2 & 0 & 0 & \dots & \dots & 0 \\ 0 & 2\beta_1+\beta_2+\beta_3 & 0 & -\beta_2 & 0 & \dots & \dots & 0 \\ -\alpha_2 & 0 & 2\alpha_1+2\alpha_2+\alpha_3 & 0 & -\alpha_2 & \ddots & \ddots & 0 \\ 0 & -\beta_2 & 0 & 2\beta_1+2\beta_2+\beta_3 & 0 & -\beta_2 & \ddots & 0 \\ \vdots & \ddots & \ddots & \ddots & \ddots & \ddots & \ddots & \vdots \\ \vdots & \ddots & \ddots & \ddots & \ddots & \ddots & \ddots & -\beta_2 \\ \vdots & \ddots & \ddots & \ddots & -\alpha_2 & 0 & 2\alpha_1+\alpha_2+\alpha_3 & 0 \\ 0 & \dots & \dots & \dots & 0 & -\beta_2 & 0 & 2\beta_1+\beta_2+\beta_3 \end{bmatrix} \tag{14}$$

$$g_2 = \begin{bmatrix} I_2^{1,1} - I_3^{1+a_{1,1}^2,1+l_{1,1}^2} & \dots & I_2^{m,n} - I_3^{m+a_{m,n}^2,n+l_{m,n}^2} \end{bmatrix} \tag{15}$$

b_t, a vector of size $4mn$, is defined as:

$$b_t = \begin{bmatrix} -\epsilon_1 & -\epsilon_2 & \dots & -\epsilon_1 & -\epsilon_2 & \epsilon_1 & \epsilon_2 & \dots & \epsilon_1 & \epsilon_2 \end{bmatrix}^T \tag{16}$$

where $\epsilon_1 = \alpha_3\gamma_a$ and $\epsilon_2 = \beta_3\gamma_l$. The adaptive regularization term b_s is defined as:

$$b_s = \begin{bmatrix} b_1 & b_2 \end{bmatrix}^T \tag{17}$$

Here, b_k ($k \in \{1, 2\}$) is a vector of size $2mn$. b_k is defined as:

$$b_k = \begin{bmatrix} b^k_{init} & b^k_{mid} & \dots & b^k_{mid} & b^k_{end} \end{bmatrix} \tag{18}$$

b^k_{init}, b^k_{mid} and b^k_{end} are vectors of size $2n$ and are defined as follows:

$$b^k_{init} = \begin{bmatrix} -(\alpha_1 + \alpha_2)\epsilon^k_a, -(\beta_1 + \beta_2)\epsilon^k_l, -\alpha_2\epsilon^k_a, -\beta_2\epsilon^k_l, \dots, \\ -\alpha_2\epsilon^k_a, -\beta_2\epsilon^k_l, -\alpha_1\epsilon^k_a + \alpha_2\epsilon^k_a, -\beta_1\epsilon^k_l + \beta_2\epsilon^k_l \end{bmatrix} \tag{19}$$

$$b^k_{mid} = \begin{bmatrix} -\alpha_2\epsilon^k_a & -\beta_2\epsilon^k_l & 0 & \dots & 0 & \alpha_2\epsilon^k_a & \beta_2\epsilon^k_l \end{bmatrix} \tag{20}$$

$$b^k_{end} = \begin{bmatrix} (\alpha_1 - \alpha_2)\epsilon^k_a, (\beta_1 - \beta_2)\epsilon^k_l, \alpha_1\epsilon^k_a, \beta_1\epsilon^k_l, \dots, \\ \alpha_1\epsilon^k_a, \beta_1\epsilon^k_l, \alpha_1\epsilon^k_a + \alpha_2\epsilon^k_a, \beta_1\epsilon^k_l + \beta_2\epsilon^k_l \end{bmatrix} \tag{21}$$

D is defined as:

$$D = \begin{bmatrix} A & B \\ B & A \end{bmatrix} \tag{22}$$

A is:

$$A = \begin{bmatrix} Q' & S' & O' & \dots & \dots & O' \\ S' & R' & S' & \ddots & \ddots & \vdots \\ O' & S' & R' & \ddots & \ddots & \vdots \\ \vdots & \ddots & \ddots & \ddots & \ddots & \vdots \\ \vdots & \ddots & \ddots & \ddots & R' & S' \\ O' & \dots & \dots & O' & S' & Q' \end{bmatrix} \tag{23}$$

$S' = diag(-\alpha_1, -\beta_1, ..., -\alpha_1, -\beta_1)$ and O' is zero matrix of size $2n \times 2n$. $B = diag(S'', S'', ..., S'')$ is a diagonal matrix of size $2mn \times 2mn$ where

$$S'' = diag(-\alpha_3, -\beta_3, ..., -\alpha_3, -\beta_3). \tag{24}$$

Q' and R' are tridiagonal matrices of size $2n \times 2n$ and are defined as Eq. 13 and 14 respectively. For a quick look-up, we have provided short definitions of the variables, parameters, vectors and matrices associated with our technique in Table 2.1. Furthermore, for a better understanding of our method, we present a flow diagram in Figure 2.3.

2.2.3 Ultrasound Simulation

The simulation phantom is generated using Field II, a commonly used ultrasound image simulator [63]. Once the phantom is generated, it is compressed by ABAQUS (Province, RI), a FEM package. The mechanical property of the simulated phantom is assumed to be homogeneous with a cylindrical inclusion with an elasticity of 0 kPa in the middle (i.e. a hole). The elasticity modulus of the background is considered to be 4 kPa. The cylindrical inclusion simulates a vein with a diameter of 8 mm which easily collapses under pressure. For simulation in Field II, the parameters of the ultrasound probe are set to values consistent with a commercial probe. The frequency of the probe is $7.27MHz$, the sampling rate is $40MHz$ and the fractional bandwidth is 60%. The number of active elements for beamforming is set to 64.

2.3 Results

For evaluating the efficacy of our algorithm, we have tested our algorithm on Finite Element Method (FEM) simulation data, a CIRS tissue-mimicking breast phantom (Norfolk,VA) and clinical data. We have compared the results with two previously published algorithms Hybrid [7] (a window-based method) and GLUE [6] (an optimization-based method). Along with qualitative comparison by inspection, we have used three conventional quality metrics Signal to Noise Ratio (SNR), Contrast to Noise Ratio (CNR) [32] and Strain Ratio (SR) to allow quantitative comparisons:

$$\text{CNR} = \frac{C}{N} = \sqrt{\frac{2(\bar{s_b} - \bar{s_t})^2}{{\sigma_b}^2 + {\sigma_t}^2}}, \text{SNR} = \frac{\bar{s}}{\sigma}, \text{SR} = \frac{\bar{s_t}}{\bar{s_b}} \tag{25}$$

where $\bar{s_b}$ and $\bar{s_t}$ are spatial strain average of background and target, ${\sigma_b}^2$ and ${\sigma_t}^2$ represent spatial variance of background and target, and $\bar{s}$ and σ denote spatial average and standard deviation of background window respectively. It is worth mentioning that windows where the underlying true strain is relatively uniform should be chosen to calculate SNR and CNR.

For simulation and phantom experiments, spatial regularization parameters α_1, α_2, β_1, β_2 are set to 5, 1, 5, 1 respectively. For *in-vivo* experiments, α_1 and β_1 are fixed at 20 while the other two spatial regularization parameters are kept the same. The temporal regularization parameters α_3 and β_3 are fixed at 20 for simulation and 1.5 for phantom and *in-vivo* experiments. For comparison purposes, results

for GLUE and Hybrid are also generated. The tunable regularization parameters for GLUE are set to the values as described in GLUE [6], which are also different for different applications. Ultrasound machines have presets for imaging different organs. For the Hybrid method, optimal results are obtained considering window size, inter-window shift, nearest neighbor factors and weighting factors of 380, 32, 5 and 0.4 respectively for simulation and phantom experiments. For *in-vivo* data, the Hybrid method produces optimal strain images when nearest neighbor factors are set to 3 while all other parameters are similar to those of simulation and phantom experiments. We incorporate three frames for our proposed method, and therefore have two axial strain fields. To keep this chapter concise, we show only one of the strain images.

2.3.1 Simulation Results

We compress the simulation phantom by a maximum of 1% with the strain between two consecutive frames set to 0.5%. While dealing with real data, we encounter various unknown types of noise. Hence it is more realistic to add random noise to simulation RF data. We add two levels of noise with uniform distribution having Peak Signal-to-Noise Ratio (PSNR) values of 18.75 dB and 10.78 dB. Figure 2.4 shows the ground truth axial strain (i.e. the FEM strain).

Along with the results for the case of no additive noise, we report the results for the aforesaid two levels of additive noise. Figure 2.5 shows the axial strain images for Hybrid, GLUE and GUEST. For all of the cases, GUEST produces visually better strain images than Hybrid and GLUE. In Figure 2.5, the inclusion edge might be diffused due to two factors: first, the regularization terms in GLUE and GUEST; second, the large kernel size of the least squares method for generating strain images from displacement estimates. Table 2.2 shows the quantitative comparison of performance among the three methods. GUEST outperforms Hybrid and GLUE in terms of SNR, CNR and SR. It is worth noting that since our inclusion in this experiment is easily deformable, higher SR value corresponds to a better strain image. The target and background windows for calculating these quantitative values are demonstrated in Figure 2.5(b).

To provide a more comprehensive view of CNR values, histograms are shown in Figure 2.5. We have moved the small blue colored window in Figure 2.5(c) within a big window to take 6 target windows. At the same time, we sweep the small red

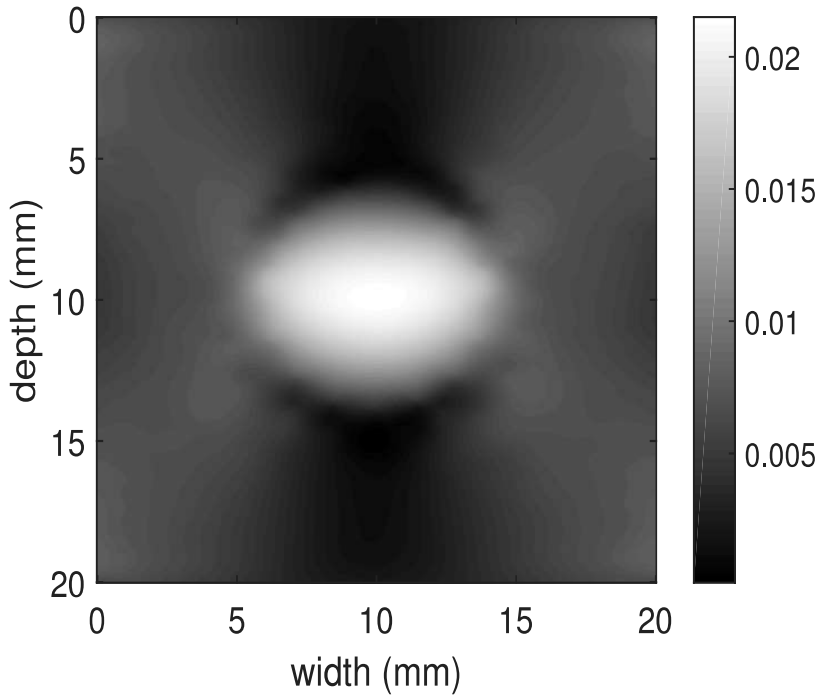

Figure 2.4: Ground truth axial strain from FEM.

colored window within 2 large windows to consider 20 background windows. We have calculated the CNR value for every combination of target and background windows, which results in 120 total combinations. The histograms for this 120 CNR values show that, at lower CNR values, GUEST has a lower frequency than the other two algorithms under consideration. The histograms show that GUEST has much higher frequencies than Hybrid and GLUE at higher CNR values. We have performed statistical analysis using the paired t-test with the aforementioned 120 CNR values. For the case of no additive noise, GLUE is statistically better than the hybrid method

Table 2.2: SNR, CNR and SR of the strain images for simulation phantom. CNR is calculated from blue colored target windows and red colored background windows depicted in Figure 2.5(b). SR is calculated on blue colored target windows and white colored background windows. SNR is calculated on red colored background windows. Elasticity moduli of inclusion and background are 0 kPa and 4 kPa respectively.

	No additive noise			PSNR = 18.75 dB			PSNR = 10.78 dB		
	SNR	CNR	SR	SNR	CNR	SR	SNR	CNR	SR
Hybrid	1.80	16.57	**3.31**	4.15	13.07	2.53	fails	fails	fails
GLUE	1.90	17.27	2.90	1.89	15.89	2.81	1.63	13.07	2.75
GUEST	**5.72**	**23.64**	3.06	**5.09**	**23.67**	**3.00**	**2.28**	**20.02**	**3.05**

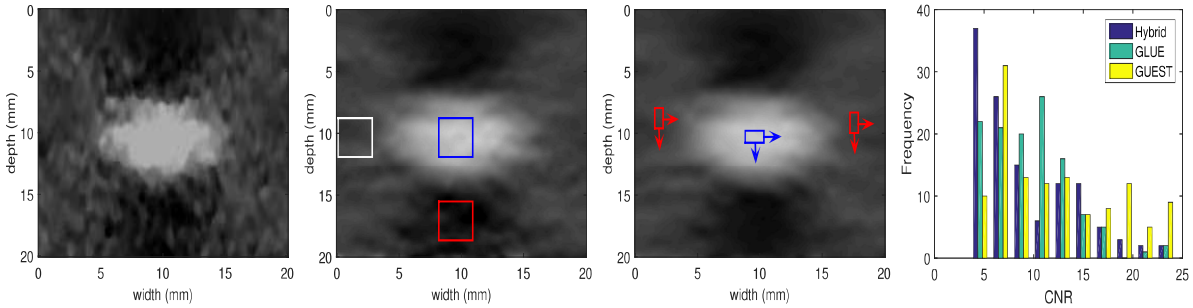

(a) Hybrid, no additive noise (b) GLUE, no additive noise (c) GUEST, no additive noise (d) Histogram of CNR values for no additive noise

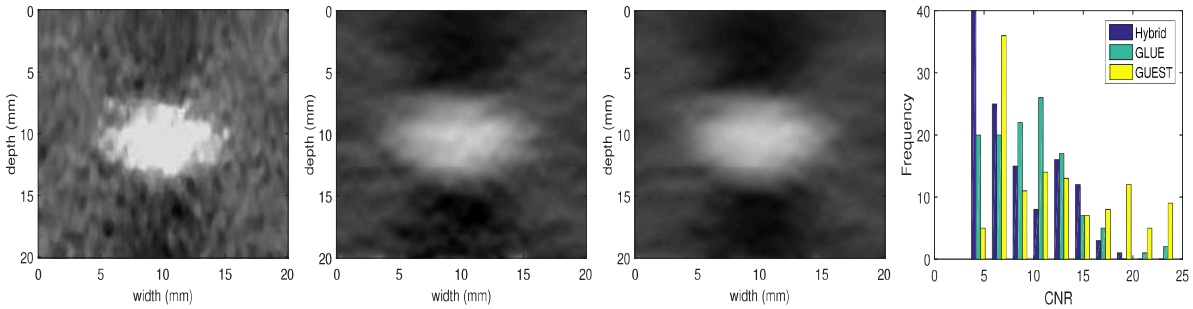

(e) Hybrid, 18.75 dB PSNR (f) GLUE, 18.75 dB PSNR (g) GUEST, 18.75 dB PSNR (h) Histogram of CNR values for PSNR of 18.75 dB

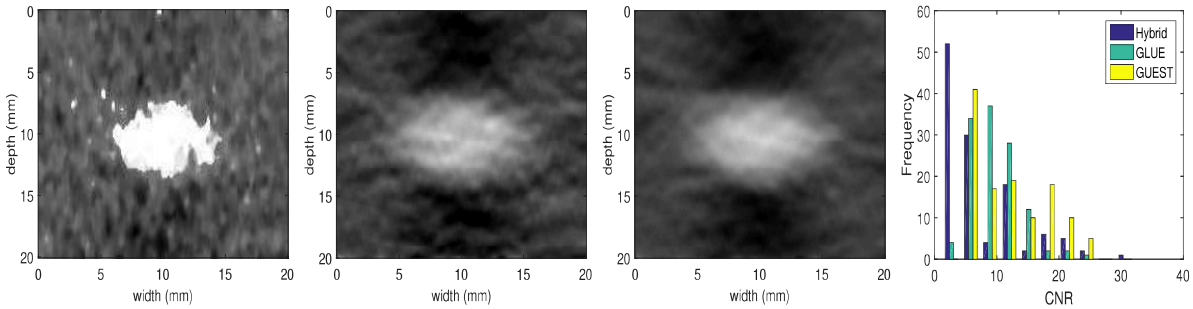

(i) Hybrid, 10.78 dB PSNR (j) GLUE, 10.78 dB PSNR (k) GUEST, 10.78 dB PSNR (l) Histogram of CNR values for PSNR of 10.78 dB

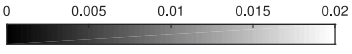

(m) Color bar

Figure 2.5: Axial strain images and histograms of CNR values for the simulation phantom. Row 1 corresponds to the case of no additive noise. Rows 2 and 3 correspond to PSNR values 18.75 dB and 10.78 dB respectively. Columns 1-3 show strain images for Hybrid, GLUE and GUEST respectively. Column 4 depicts the histograms of CNR values. (m) shows the color bar for strain images.

with a p-value of 0.2551. For this case, GUEST is statistically better than GLUE with a p-value close to zero. For both PSNR values of 18.75 dB and 10.78 dB, GLUE is statistically better than the hybrid method with p-values close to zero. In addition, GUEST statistically outperforms GLUE with p-values nearly zero.

2.3.2 Experimental Results

The phantom experiment was carried out at PERFORM centre, Concordia Univeristy. RF data was collected using an E-Cube R12 research ultrasound machine with an L3-12H linear array probe at the center frequency of $10MHz$ and sampling rate of $40MHz$. Clinical data was collected at Johns Hopkins Hospital from a research Antares Siemens system at $6.67MHz$ center frequency with a VF 10-5 linear array at a sampling rate of $40MHz$.

Phantom Results

Compression was performed on a tissue-mimicking breast phantom made from Zerdine® (Model 059, CIRS: Tissue Simulation & Phantom Technology, Norfolk, VA) with Young's elasticity modulus of 20 ± 5 kPa corresponding to the background, which mimics the ultrasound reflective properties of average human breast. The elasticity modulus of the spherical hard inclusion is at least twice as large as the modulus of the background. Three consecutive frames are selected to generate axial strain images. Axial strain images for phantom data are provided in Figure 2.6. Quantitative values of image quality in terms of SNR, CNR and SR are represented in Table 2.3. CNR is calculated between white colored target windows and red colored background windows, whereas SR is calculated from white colored target windows and blue colored background windows (shown in Figure 2.6(b)). SNR is calculated for background windows only. It is clear that GUEST produces less noisy images with sharper edges. SNR and CNR values support our visual assessment by showing substantially higher numbers for GUEST compared to both the hybrid method and GLUE. In this experiment, the inclusion being stiffer than the background, the better strain image provides a lower SR value. Hence, according to Table 2.3, SR values depict the fact that GUEST outperforms Hybrid and GLUE.

Similar to the simulation experiment, we have calculated CNR values for 120 combinations of target and background windows (6 target and 20 background windows) shown in Figure 2.6(c). We show the histogram with the CNR values in Figure 2.6(d).

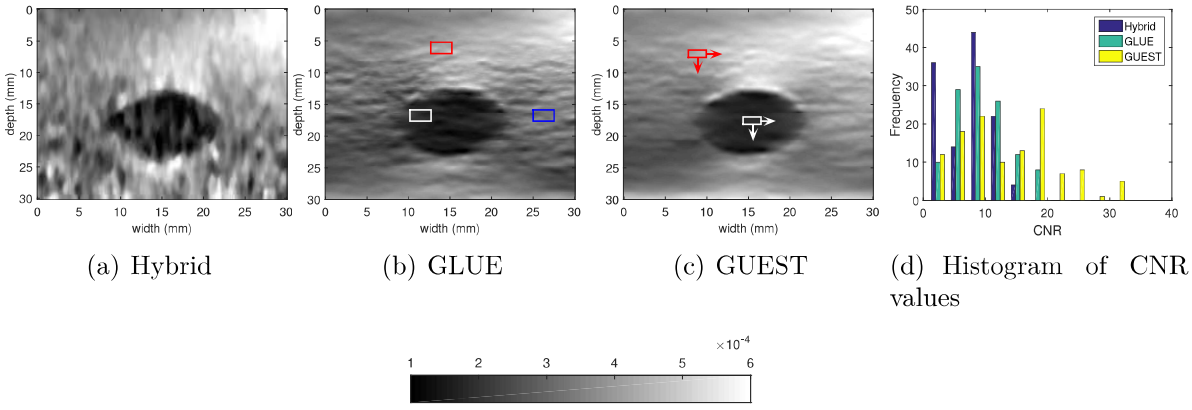

(a) Hybrid (b) GLUE (c) GUEST (d) Histogram of CNR values

(e) Color bar

Figure 2.6: Axial strain images and histogram of CNR values for the CIRS breast elastography phantom. Columns 1 to 3 show strain images for Hybrid, GLUE and GUEST respectively. Column 4 represents the histogram of CNR values. (e) represents the color bar.

Table 2.3: SNR, CNR and SR of the strain images for experimental phantom. CNR is calculated from white colored target windows and red colored background windows depicted in Figure 2.6(b). SR is calculated between white colored target windows and blue colored background windows. SNR is calculated on red colored background windows.

	SNR	CNR	SR
Hybrid	16.26	3.11	0.79
GLUE	15.51	5.44	0.72
GUEST	**19.91**	**6.51**	**0.65**

GUEST has higher frequency in higher CNR values and lower frequency in relatively lower CNR values. This complete quantitative analysis of the overall image shows that GUEST performs better than GLUE and Hybrid. To compare different methods, we performed paired t-test. GLUE statistically outperforms the hybrid method with a p-value close to zero. In addition, GUEST is statistically better than GLUE with a p-value in the vicinity of zero.

In-vivo Results

For the clinical study, *in-vivo* data were collected from three patients undergoing open-surgical RF thermal ablation for liver cancer at Johns Hopkins Hospital. Full details of the experimental procedure are elaborated in [5]. The study was approved by the institutional review board and informed consent was obtained from all patients.

For the administration of RF ablation, RITA Model 1500 XRF generator (Rita Medical Systems, Fremont, CA) was used. The tissue was compressed simply by pushing the probe against the liver with the hand-held probe at a frequency of approximately 1 compression per 2 sec. The location of the tumor and the small surgical opening resulted in compressions with substantial out-of-plane motion of the probe. Furthermore, hepatic blood flow and other biological sources introduced additional sources of noise.

The B-mode and strain images for patient 1 are shown in Figure 2.7. GLUE and GUEST provide substantially better visualizations of the tumor compared to the B-mode image. From Table 2.4, one can see that GUEST outperforms both the hybrid method and GLUE. Target and background windows for quantitative comparison are shown in Figure 2.7(c). Figure 2.8 presents B-mode and strain images for patient 2. The strain image from GUEST is less noisy than for the hybrid method and GLUE. Although the Hybrid method provides the most noisy strain image, it might show lesion boundary more clearly. This clearer lesion boundary could be due to the post-processing steps performed in the Hybrid method. The values in Table 2.4 show that GUEST substantially outperforms both the hybrid method and GLUE in terms of SNR, CNR and SR. Target and background windows for calculating SNR and CNR are marked in Figure 2.8(b) while target and background windows for calculating SR are indicated in Figure 2.8(c).

Similar to the simulation and phantom experiments, the histogram analysis for 120 CNR values (6 blue target and 20 red background windows shown in Figure 2.7(d) and Figure 2.8(d)) is performed for data both from patient 1 and patient 2 (Figure 2.7(e) and Figure 2.8(e)). In both cases, most high CNR values are observed with GUEST. For CNR values obtained from patient 1, GLUE performs statistically better than the hybrid method with a p-value nearly zero. GUEST statistically outperforms GLUE with a p-value around zero. For 120 CNR values from patient 2, GLUE is statistically better than the hybrid method with a p-value of 5.2270×10^{-5}. GUEST is better than GLUE with a p-value close to zero.

B-mode and axial strain images for patient 3 from GLUE and GUEST are depicted in Figure 2.9. This figure shows that GUEST provides a better visualization of the stiffer region of the tissue than GLUE. Quantitative values of SNR, CNR and SR in Table 2.5 agree with the visual assessment. Target and background windows for quantitative evaluation are shown in Figure 2.9(b). As the hybrid method fails to estimate the displacement map, we report the results from GLUE and GUEST only.

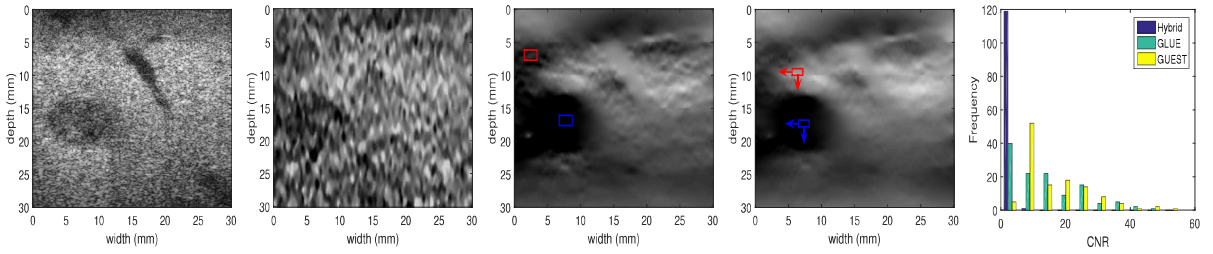

(a) B-mode (b) Hybrid (c) GLUE (d) GUEST (e) Histogram of CNR values

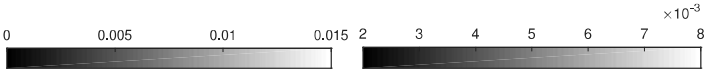

(f) Color bar for Hybrid (g) Color bar for GLUE and GUEST

Figure 2.7: Results of *in-vivo* data from patient 1. (a) represents the B-mode image. (b)-(d) show strain images for Hybrid, GLUE and GUEST respectively. The tumor is clearly visible as a dark region in (c) and (d). (e) shows the histogram of CNR values. (f) represents the color bar for Hybrid whereas (g) shows the color bar for GLUE and GUEST.

Table 2.4: SNR, CNR and SR of the strain images of patients 1 and 2. CNR and SR are calculated from blue colored target windows and red colored background windows depicted in Figures 2.7(c), 2.8(b) and 2.8(c), and SNR is calculated on red colored background windows.

	Patient 1			Patient 2		
	SNR	CNR	SR	SNR	CNR	SR
Hybrid	2.18	1.16	1.50	11.36	7.78	0.98
GLUE	13.21	5.81	0.67	21.59	4.97	0.61
GUEST	**21.53**	**9.67**	**0.64**	**26.99**	**10.52**	**0.54**

Histogram (Figure 2.9(d)) for 120 CNR values (6 blue target and 20 red background windows shown in Figure 2.9(c)) from patient 3 shows that most of the higher CNR values belong to GUEST. Statistically, GUEST is better than GLUE with a p-value close to zero.

2.3.3 Computation Time

We have implemented our algorithm on a 4^{th} generation 3.6 GHz Intel core-i7 PC. The other two methods (hybrid and GLUE) were also executed on the same computer. MATLAB R2015a platform was used for the implementation. For three conventional ultrasound frames of size 1000×100, the computation time of two displacement fields (frame 1 to 2 and frame 2 to 3) are reported in Table 2.6.

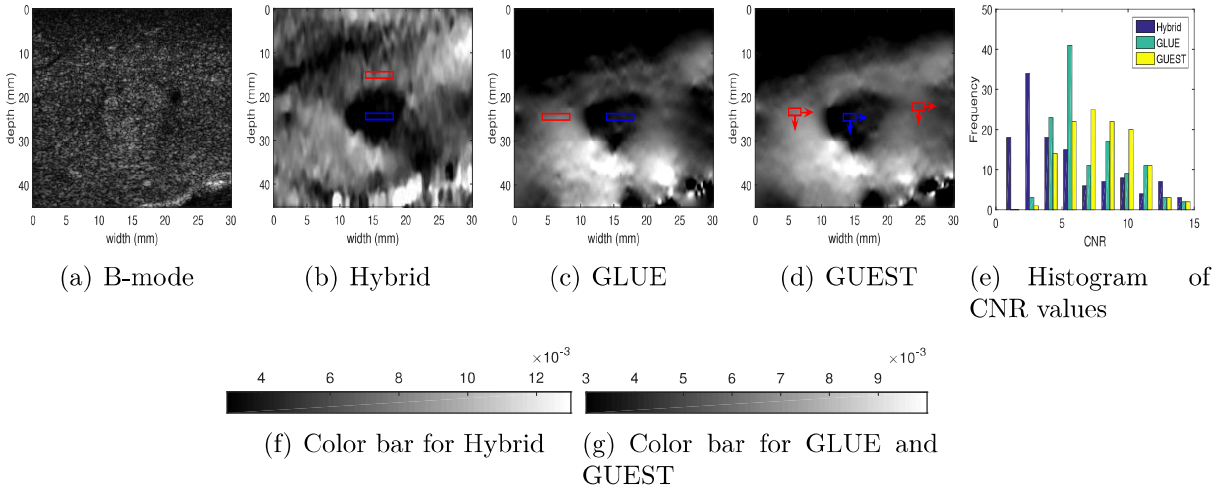

(a) B-mode (b) Hybrid (c) GLUE (d) GUEST (e) Histogram of CNR values

(f) Color bar for Hybrid (g) Color bar for GLUE and GUEST

Figure 2.8: Results of *in-vivo* data from patient 2. (a) represents the B-mode image. (b)-(d) show strain images for Hybrid, GLUE and GUEST respectively. (e) depicts the histogram of CNR values. (f) represents the color bar for Hybrid whereas (g) shows the color bar for GLUE and GUEST.

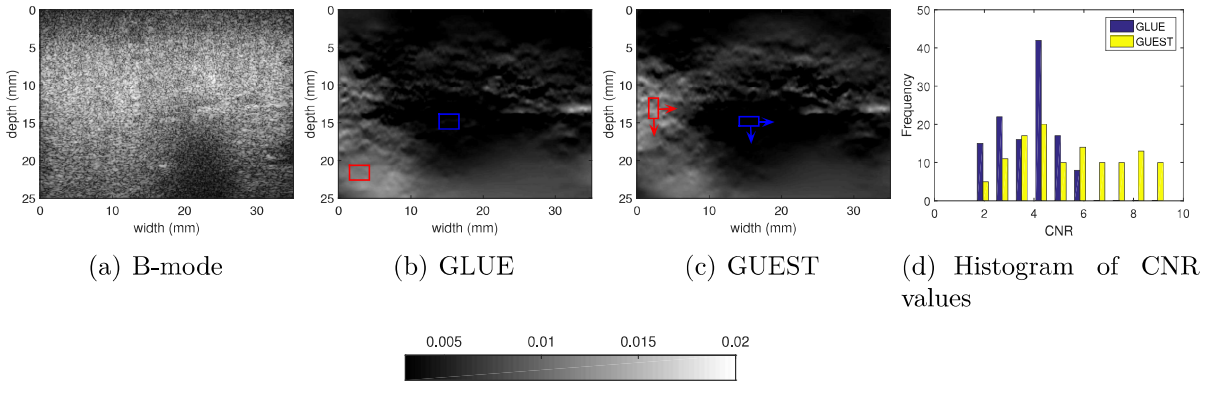

(a) B-mode (b) GLUE (c) GUEST (d) Histogram of CNR values

(e) Color bar

Figure 2.9: Results of *in-vivo* data from patient 3. (a) represents the B-mode image. (b) and (c) show strain images for GLUE and GUEST respectively. (d) depicts the histogram of CNR values. (e) represents the color bar for strain images.

Table 2.5: SNR, CNR and SR of the strain images of patient 3. CNR and SR are calculated with blue colored target windows and red colored background windows depicted in Figure 2.9. SNR is calculated on red colored background windows.

	SNR	CNR	SR
GLUE	21.75	10.96	0.22
GUEST	**25.09**	**14.36**	**0.14**

Table 2.6: Computation time of two displacement fields between three ultrasound frames of size 1000×100.

	Time (seconds)
Hybrid	96.91
GLUE	1.34
GUEST	1.77

It is evident that GLUE and GUEST show much better timing performance than hybrid method. Although GUEST is slightly more expensive than GLUE, execution time can be reduced by implementing GUEST with the MATLAB MEX function. In addition to that, using GPU instead of CPU can accelerate the algorithm dramatically.

2.4 Discussion

It is shown in DPAM [5] and GLUE [6] that spatial regularization improves time delay estimation by reducing the effect of signal decorrelation. As ultrasound machines can collect data at a very high rate, displacement of a speckle from frame 1 to frame 2 and frame 2 to frame 3 should not be very different and hence temporal continuity is also an important property which can be utilized in improving displacement estimation. The extent of temporal regularization is slightly tissue dependent. A rule of thumb is that a large regularization weight is needed for data collected at very high rate for imaging an organ which is expected to have a smooth displacement field. Otherwise if the tissue deforms quickly and in a complicated manner, a moderate regularization weight is preferred. In this work, the optimum value for the temporal regularization parameter was achieved by manual tuning. These values can be stored for imaging different types of tissue as pre-sets. A similar approach is commonly utilized in commercial ultrasound machines which have some imaging parameters that are embedded

in the pre-settings for imaging different organs.

Free-hand palpation elastography is performed by pressing the tissue with a hand-held probe, which results in probe motion in all possible six degrees of freedom (three rotations and three translations). In this work, we select RF frames that exhibit mostly axial deformations by visual inspection. Since the probe velocity, which resembles a sinusoidal function, is not constant, the average strain levels between consecutive frames is different. This issue is addressed by making the temporal continuity term adaptive. As the difference of two consecutive initial displacement estimates is averaged over many samples using a Gaussian kernel to obtain the temporal adaptation terms, low variance estimates of the acceleration are utilized in the temporal regularization term.

As reported in [5], spatial regularization may result in underestimation of displacement field due to tissue inhomogeneity. However, this issue was not taken into account in GLUE. Adaptive spatial regularization makes the proposed method (GUEST) capable of preventing such underestimation of displacement.

Memory usage is always an important concern while dealing with ultrasound RF frames, and is even more important when more than two frames are incorporated for TDE. In our work, the coefficient matrix is of size $4mn \times 4mn$ for 3 consecutive frames of size $m \times n$, requiring a prohibitive amount of memory for RF frames of conventional size. For example, the size of the coefficient matrix will be 400000×400000 for 3 ultrasound frames of size 1000×100, which requires a memory of few hundred gigabytes. But, the matrices used in our method are band matrices whose non-zero entries are confined to diagonal bands. Hence during implementation, treating the aforementioned matrices as sparse allowed us to limit the memory requirement to approximately $100MB$.

As incorporating more than two frames in ultrasound elastography is unconventional, it may advocate the impression that employment of more frames keeps improving the result. However, as more frames are included, the time-delay from the reference frame also increases which may further introduce signal decorrelation noise. Computational cost is another factor which increases substantially along with the addition of new frames. Taking these two points into consideration, the optimal number of frames is an interesting avenue of further investigation.

State-of-the-art ultrasound imaging techniques have been proposed with plane-wave imaging in several applications such as vascular and cardiac imaging. The quality of ultrasound images is usually sacrificed to some extent to achieve higher frame rates.

As such, temporal regularization can be a very powerful tool for these applications to produce more accurate tracking results.
Any regularization may increase estimation bias, which may lead to strain images with lower contrast. However, the results presented in this chapter show that GUEST maintains a bias-variance trade-off by improving both SNR and CNR. In each experiment, we calculated CNR in 120 windows and showed that GUEST provides a substantially higher CNR. In addition to this, we report results for both a soft inclusion (simulation experiment) and hard inclusions (phantom and *in-vivo* experiments). Our method obtains optimal results for both cases.

2.5 Summary

In this chapter, we proposed GUEST: Global Ultrasound Elastography in Spatial and Temporal domains. We utilized information on continuity of displacement field in the temporal direction to reduce the variance of the estimated displacement field. We used three frames of RF data to formulate a cost function that is regularized both spatially and temporally. This cost function had more than a million variables and was highly nonlinear. We simplified this complex optimization problem into a sparse linear system of equations and showed that it can be efficiently solved, which makes it an attractive technique for real-time implementation on commercial ultrasound machines. We showed using simulation, phantom and *in-vivo* experiments that GUEST substantially outperforms two recent ultrasound elastography techniques.

Chapter 3

Low Rank and Sparse Decomposition of Ultrasound Color Flow Images for Suppressing Clutter in Real-Time

In this chapter, a novel technique for real-time clutter rejection in ultrasound Color Flow Imaging (CFI) is proposed. Suppressing undesired clutter signal is important because clutter prohibits an unambiguous view of the vascular network. Although conventional eigen-based filters are potentially efficient in suppressing clutter signal, their performance is highly dependent on proper selection of a clutter to blood boundary which is done manually. Herein, we challenge the state-of-the-art techniques to resolve this limitation by formulating the clutter suppression problem as a foreground-background separation problem to extract the moving blood component. To that end, we adapt the fast Robust Matrix Completion (fRMC) algorithm, and utilize the in-face extended Frank-Wolfe method to minimize the rank of the matrix of ultrasound frames. Our method automates the clutter suppression process, which is critical for clinical use. We name the method RAPID (**R**obust m**A**trix decom**P**osition for suppress**I**ng clutter in ultrasoun**D**) since the automation step can substantially streamline clutter suppression. The technique is validated with simulation, flow phantom and two sets of *in-vivo* data. Similar to our previous work, we will release our code as well as almost all of our data online.

3.1 Introduction

Delineating the vasculature and measuring blood flow velocity in order to examine the physiological condition of the local tissue has seen a growing interest during the past few years. Visualizing the vascular structure is immensely important because architectural change in the vascular network may indicate tissue and cell damage leading to ischemia [12], diabetes related diseases [11, 64, 65] and coronary heart disease [14, 66, 67]. Aneurysms which appear on the ventricular or atrial vessels may lead to fatal heart attacks [13, 68]. An increased size of the aneurysm might be a potential source of uncontrollable bleeding in the circle of Willis of the brain, abdominal aorta and thoracic aorta [69–71]. Furthermore, the gradual development of malignant cells from benign tumors is highly affected by angiogenesis, the physiological process of development of new blood vessels from pre-existing ones [72–74]. Visualizing and monitoring of such microscopic change in early stages is of immense importance to warrant better treatment outcomes.

Ultrasound Color Flow Imaging (CFI) is an easy-to-use and cost-effective modality that can be used to observe the blood flow direction and velocity across various vascular networks in the body. The color encoded information in this modality can then be analyzed to determine any potential abnormalities in the region of interest (ROI). However, ultrasound suffers in its ability to produce a clear visualization of the ROI due to scattering of the ultrasound beam from clusters of red blood cells. In addition, clutter signals originating from stationary or slowly moving tissue components and wave reverberations are the biggest hindrances to visualizing microvascular changes. This is due to the fact that backscattered signals from blood and other tissue exhibit similar properties, especially when blood is moving slowly or tissue is moving rapidly [22, 75, 76]. Since the backscattered signal from the normal tissue is usually 40 to 100 dB stronger than that of blood [75], it dominates the signal component resulting from moving Red Blood Cell (RBC) speckles [16] which negatively affects the vessel visualization process. Another important fact is that blood and clutter components possess non-overlapping frequency spectra [22].

The backscattered signal from tissue has a lower Doppler shift than that of blood as tissue velocity is usually slower [75]. This led to using high pass filtering as a promising tool for clutter filtering in the early stages of Color Flow Imaging (CFI) research. Many methods have been developed to optimally reject unexpected clutter signals from the desired blood components [77–79]. Clutter suppression techniques based on

high pass filtering can be divided into two broad classes: Finite Impulse Response (FIR) filters [15] and Infinite Impulse Response (IIR) filters [16]. Each of the classes has its own advantages and downsides. Despite having a steeper roll-off, IIR filters suffer from longer settling time [22]. In contrast, FIR filters minimize the settling time, but require a higher order to separate clutter component from blood signal. However, FIR and IIR filters share a common problem of having inadequate slow-time samples leading to ineffective classification of data generated from slowly moving soft tissue and blood [19,76]. In addition, in cases where unexpected tissue movement dominates, high pass filters fail to adaptively select the filter cut-off frequency based on clutter characteristics [76].

To resolve the issue of proper cut-off selection, several eigen-based filtering methods have been proposed to discriminate clutter and blood [17, 19–21]. The underlying assumption prompting the development of eigen-based techniques is that tissue is spatio-temporally more coherent than blood [22]. The principal idea is to discard the eigen subspace representing the clutter component in the slow-time signal [76]. Initially, one-dimensional spatial and temporal information was taken into account to filter out the clutter signal [18, 80]. These one-dimensional approaches fail to distinguish tissue subspace from blood subspace when the speed of blood is low or the tissue motion is faster than normal [22].

To address the aforementioned shortcomings of one-dimensional investigation, Singular Value Decomposition (SVD) and Principal Component Analysis (PCA) of a large Casorati matrix [81] consisting of 2D spatial and temporal coherence [22] has been proposed. Along similar lines, recent work proposed processing the power Doppler images obtained from SVD using Non-local mean based framework, morphological filtering and Hessian-based vessel enhancement techniques [82–84]. In addition, motion correction of the acquired ultrasound frames has been introduced to improve the sensitivity of power Doppler imaging [85]. The eigen-based filter has been extended to the 3^{rd} dimension in [23,86,87] using the higher order SVD technique [88]. However, determining the threshold value that separates blood from normal tissue is challenging in this method. More specifically, it is assumed that the first few eigen-values are associated with clutter, the next few represents blood, while the rest denote noise [23]. The dimensions of clutter and blood are manually chosen to reject clutter and noise [23]. Having no rigid ground to determine the dimension of clutter, this manual approach is prone to inefficient suppression of clutter. Therefore, recent work [89] proposed 5 parametric and 5 non-parametric methods to select the

boundary between clutter and blood subspaces.

To address the aforementioned limitations of PCA- and SVD-based techniques, we propose to look at the clutter suppression problem from the viewpoint of decomposing the data matrix into low rank and sparse components in a computationally efficient manner. The decomposition makes use of the Robust Matrix Completion algorithm, where the low rank component represents the steady tissue signal and the sparse component represents the moving blood echo. More specifically, we organize a series of acquired ultrasound RF frames into a data matrix. Since an ultrasound RF frame contains some measure of echo for each of its sample, the data matrix is complete with no missing element. Therefore, the Robust Matrix Completion Algorithm acts like Robust Principal Component Analysis (RPCA) [90, 91]. Comprehensive studies [92–95] have been conducted during the last few years to resolve the matrix rank minimization problem. Many of these algorithms [90, 96] have been successful in the field of computer vision to separate the foreground from the background resulting in automatic separation of foreground and background. However, these techniques are computationally very expensive and also have high memory requirement.

Herein, our goal is to consider blood as the foreground since it is the rapidly moving component, and clutter as the background. Instead of using computationally expensive and memory exhaustive RPCA methods, we have adapted the recently proposed fast Robust Matrix Completion (fRMC algorithm) [24] and the in-face extended Frank-Wolfe method [25] for the purpose of separating the blood component from the stationary tissue echo. As such, we call the algorithm RAPID (**R**obust m**A**trix decom**P**osition for suppress**I**ng clutter in ultrasoun**D**). RAPID is briefly illustrated in Figure 3.1. The main advantage of RAPID is that there is no need to select any threshold manually to separate the blood and clutter components.

We have validated our technique with simulation, flow phantom, *in-vivo* rat and human datasets. The RF data of the phantom experiment and the *in-vivo* rat dataset collected for this work will be publicly available. Additionally, we will publicly release the MATLAB code of RAPID, similar to our previous work [6, 26].

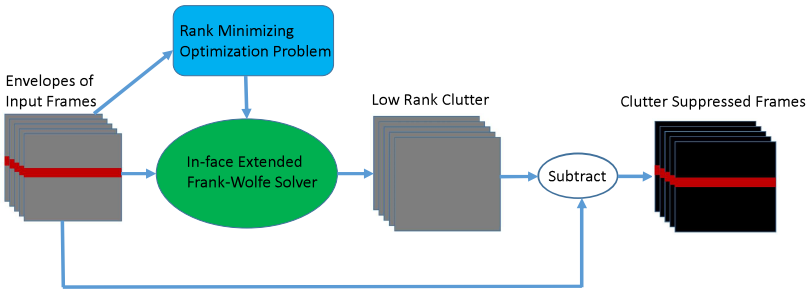

Figure 3.1: A flowchart of the proposed RAPID algorithm.

3.2 Experimental set-up and data acquisition

3.2.1 Design and Materials for Phantom Experiment

The phantom gel is created from a mixture of water, Knox unflavored gelatin, sugar-free Metamucil psyllium fiber supplement [97], and a container to store the mixture. The venous structure model consisted in an intra-venous (IV) tube passed through a container which has two holes bored on parallel faces of the container. Once the gel mixture is made, it is allowed to congeal and solidify overnight. The solidified gel is then placed in a bain-marie to heat the mixture so that it can liquefy without burning, and is slowly poured into a container with the IV tube, and placed in the refrigerator to solidify.

Design and Implementation of the Flow Circuit

The flow circuit is designed to have the fluid of choice flow through the venous structure model at a desired flow rate. The circuit is a closed system, as all the liquids being pumped from the main reservoir returns back to it after having traversed the various channels of the system. The oncoming flow is produced by a siphon pump and controlled by a stopper valve. For the first two phantom experiments, our fluid of choice was water with small amounts of oil and detergent mixed in to create small scatterers. For the third and fourth phantom experiments, we used Blood Mimicking Fluid (CIRS: Tissue Simulation & Phantom Technology, Norfolk, VA). Figure 3.2 shows the experimental set-up.

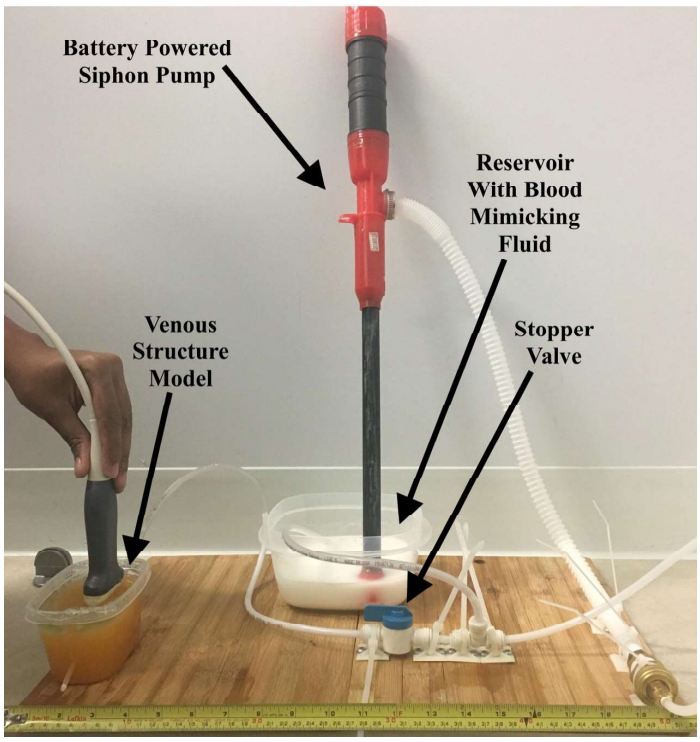

Figure 3.2: Data acquisition from the flow phantom with a hand-held L3-12H linear array probe.

3.2.2 Simulation of Ultrasound Data

We simulated a tissue with dimensions 3.6 $cm \times 2$ $cm \times 1$ cm containing a horizontal blood vessel (i.e. perpendicular to the direction of ultrasound wave propagation) of 0.4 cm diameter in the middle using the Field II software package [63, 98]. The flow was laminar with a parabolic velocity profile with the peak velocity of 25 cms^{-1}. The frame-rate of ultrasound was set to 1000 fps. The elements of the probe had a width and height of 0.02 cm and 0.5 cm with a kerf of 0.002 cm. The sampling frequency was set to 40 MHz whereas the frequency of the probe and fractional bandwidth were 7.27 MHz and 60% respectively, unless otherwise specified. For beamforming, 64 active elements were used.

3.2.3 Ultrasound Data Collection

Ultrasound RF data collections were conducted using an Alpinion E-Cube R12 research ultrasound system with an L3-12H linear array probe. In all experiments, the frequency of the probe and the sampling frequency were set to 10 MHz and 40 MHz,

(a) L3-12H Linear Array Probe with Bandwidth = 3 – 12 MHz Footprint = 4.5 cm

(b) *In-vivo* data acquisition from a gas-anesthetized male rat

Figure 3.3: Data acquisition from the abdomen of a Sprague-Dawley male rat with a hand-held L3-12H linear array probe. 20 RF frames are collected from one rat.

respectively, unless otherwise specified.

The *in-vivo* experiment on rat was carried out at the Animal Care Facility (ACF) of Concordia University. A 27 week old, Sprague-Dawley male rat was anesthetized before scanning. The rat was placed on a surgery table in supine position as shown in Figure 3.3. A portion of the abdominal hair was shaved to prevent large attenuation of waves in the hair. Ultrasound RF data was collected from the abdomen of the rat using the L3-12H linear array probe by conventional focused beamforming. All procedures were approved by the Animal Ethics Committee of Concordia University (#30000259) and were conducted in accordance with guidelines of the Canadian Council on Animal Care.

The human-subject data was collected from the knee of a volunteer using a hand-held probe at Concordia University's PERFORM Centre. The data collection was conducted with an approved ethics from Quebec's Ministere de la Sante et des Services (MSSS).

3.3 Methods

Assume that we have p ultrasound RF frames of size $m \times n$. The complex envelopes of the RF frames are denoted by $E_i \in \mathbb{C}^{m \times n}$ where $i \in \{1, 2, 3, \ldots, p\}$. All p envelopes

are organized in a data matrix $D \in \mathbb{C}^{mn \times p}$ where each column represents the complex envelope of an RF frame. Our purpose is to separate blood and clutter subspaces from the data matrix D. In this section, we first briefly describe the conventional SVD-based algorithm [22], and then elaborate the proposed method.

3.3.1 SVD Clutter Suppression

In this method, the data matrix D is decomposed as:

$$D = U\Sigma V^{\dagger} = \sum_{l=1}^{r} \sigma_l u_l v_l^{\dagger} \tag{26}$$

where $U \in \mathbb{C}^{mn \times mn}$ and $V \in \mathbb{C}^{p \times p}$ are unitary matrices containing the left and right singular vectors of D respectively. $\Sigma \in \mathbb{R}^{mn \times p}$ is a diagonal matrix with diagonal entries set to the singular values of D. $r = \min(mn, p)$ denotes the rank of the matrix D. σ_l, u_l and v_l stand for singular values and left and right singular vectors of D, respectively. Superscript † denotes the conjugate transpose.
Since mn is usually a very large number, the matrix U cannot be stored in memory of conventional computers (for typical RF signals and $p = 20$ frames, approximately 500 GB of RAM is required to store U). Therefore, only the first $mn \times p$ elements of U are calculated and stored in memory instead of all $mn \times mn$ elements. Similarly for Σ, only the first $p \times p$ elements are calculated and stored in memory. This will lead to a significant reduction in running time and memory requirement. Once the ranks of clutter and blood subspaces c and b are found by manual tuning, the blood subspace is separated from the clutter by:

$$\hat{B} = \sum_{l=c+1}^{c+b} \sigma_l u_l v_l^{\dagger} \tag{27}$$

where $\hat{B}$ represents the blood component of the data matrix. The magnitude of every column of $\hat{B}$ or the power contained in the filtered data can be shown to depict the vasculature.

3.3.2 RAPID: Robust Matrix Decomposition in Ultrasound Clutter Suppression

If the correlation coefficient between any two of the p frames is high, the data matrix D can be modelled as a low rank matrix. The blood flow prevents having correlation between entire frames, which can be removed from the data matrix D by solving the following optimization problem [90]:

$$\min\ rank(C) \qquad \text{s.t.} \quad D = C + B$$

where C is the low rank clutter subspace and B denotes the sparse blood component. To solve the optimization problem, we consider the Low Rank Matrix Completion (LRMC) technique where sparsity of the blood component is enforced by solving the following minimization problem:

$$\min\ \|C - D\|_F^2 \qquad \text{s.t.} \quad \|C\|_\star < \delta$$

where $\|.\|_F$ represents the Frobenius norm defined as root sum squared of magnitudes of the matrix entries. $\|.\|_\star$ stands for the nuclear norm of a matrix referring to the sum of its singular values. δ is the radius of the nuclear norm ball of low rank clutter matrix C. Since D is a non-singular matrix and contains envelopes of RF frames in each column, it usually has a large Frobenius norm. Hence the square of the Frobenius norm of D which is defined as the sum of the square of the singular values is greater than the nuclear norm of D. It is mathematically impossible for the nuclear norm of C to be larger than that of D, since C is the underlying low rank component of D. Hence the upper bound of the nuclear norm ball δ can comfortably be set to any value greater or equal to the square of the Frobenius norm of D. In all of our validation examples, we set δ to ten times the square of the Frobenius norm of D. Therefore, RAPID has no tunable parameter.

This is a convex optimization problem [24, 99], which can be efficiently solved by using the recently proposed in-face extended Frank-Wolfe method [25]. It is shown in this work that the low rank structures lie in the boundary of the solution space (Figure 3.4), which is exploited to substantially increase the convergence speed and reduce the memory requirements. The algorithm is outlined in Algorithm 1.

The output of this algorithm is the optimal low rank clutter matrix C^*. However, our goal is to find the sparse blood component, which can be obtained by subtracting C^* from D. Every column of B^* $(= D - C^*) \in \mathbb{C}^{mn \times p}$ contains the sparse blood

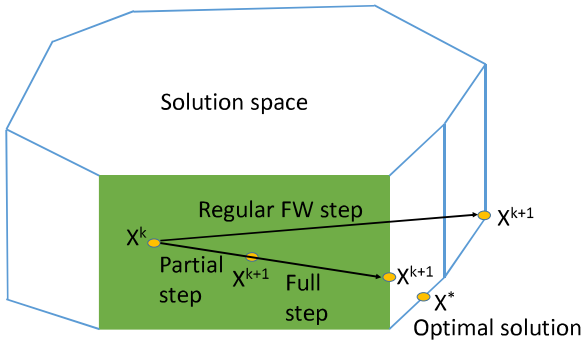

Figure 3.4: An illustration of regular and in-face steps of the in-face extended Frank-Wolfe method.

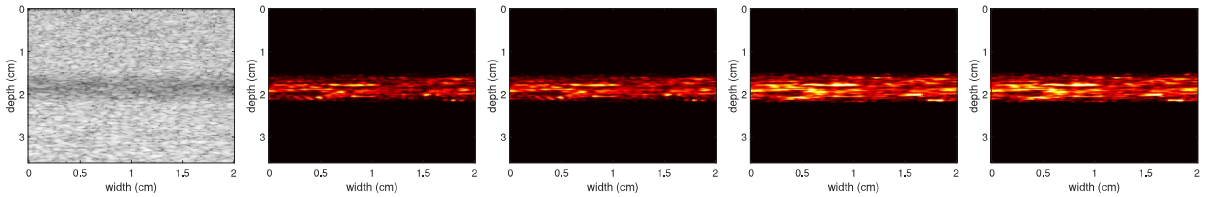

(a) B-mode (b) SVD with $c = 2$, $b = 5$ (c) SVD with $c = 2$, $b = 10$ (d) SVD with $c = 1$, $b = 15$ (e) RAPID

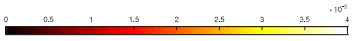

(f) Color bar

Figure 3.5: Results of the simulation experiment. Column 1 represents the B-mode image. Columns 2, 3 and 4 depict the power Doppler images from SVD with different combinations of clutter and blood subspace ranks. Column 5 shows the power Doppler image from RAPID. (f) represents the color bar for the power Doppler images.

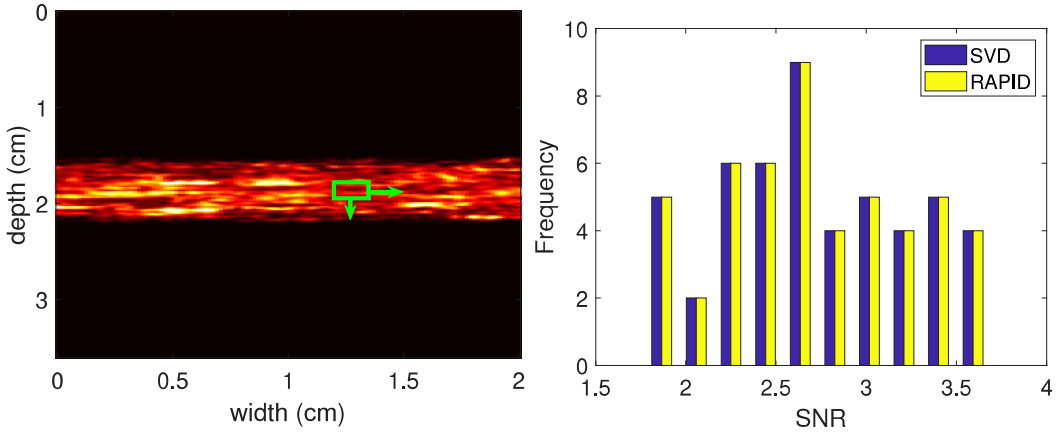

(a) Power Doppler image (b) Histogram of SNR values

Figure 3.6: Histogram of SNR values for the simulation experiment. SNR values are calculated on 50 different positions of the moving window shown in the left image.

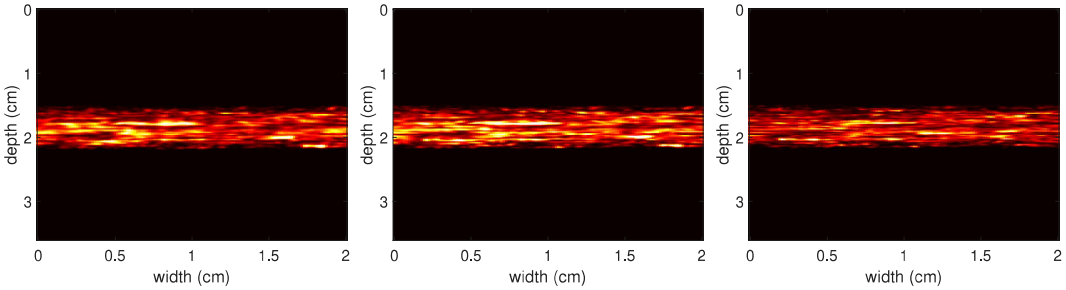

(a) SVD for 7.27 MHz center frequency

(b) SVD for 8.5 MHz center frequency

(c) SVD for 10 MHz center frequency

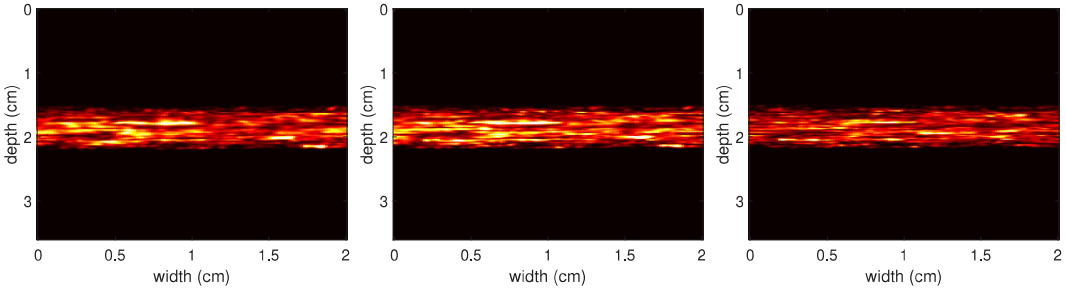

(d) RAPID for 7.27 MHz center frequency

(e) RAPID for 8.5 MHz center frequency

(f) RAPID for 10 MHz center frequency

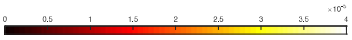

(g) Color bar

Figure 3.7: Results of the simulation experiment for different center frequencies. Columns 1-3 correspond to center frequencies of 7.27 MHz, 8.5 MHz and 10 MHz respectively. Rows 1 and 2 correspond to SVD and RAPID respectively. (g) shows the color bar for the power Doppler images.

Algorithm 1: In-face extended Frank-Wolfe algorithm for finding the low-rank clutter subspace

Input : Data matrix D and maximum number of iterations
Output: Optimal low-rank clutter subspace C^*

Definition: C^q is the current iterate of the low rank clutter matrix, $f(C^q) = \frac{1}{2}\|C^q - D\|_F^2$;
while *not converged* **do**
    Calculate $\nabla f(C^q)$: the gradient of $f(C^q)$;
    Compute the direction of next iterate d^q;
    Compute the step size;
    Compute C^{q+1}: check two conditions to determine whether to take full or partial in-face step. If none of the conditions is satisfied, take regular Frank-Wolfe step.
end

component of individual frames. B^* can be decomposed into p complex frames of size $m \times n$. The magnitude of each of these frames B_i^* can be shown as different images to visualize frame to frame flow. The power Doppler image can be generated with the magnitudes of all p clutter suppressed frames which depicts only the vasculature, not the flow:

$$P(j,k) = \frac{1}{p}\sum_{i=1}^{p}|B_i^*(j,k)|^2 \tag{28}$$

The in-face extended Frank-Wolfe solver offers a substantially faster convergence rate compared to traditional RPCA methods because it does not need to perform SVD in each iteration [25], which leads to significant reductions in its memory footprint and computational complexity. In addition, this solver calculates three directions namely full step, partial step and regular Frank-Wolfe (FW) steps (see the illustration in Figure 3.4) for updating the solution in each iteration. A full step is an in-face step suggesting to go to a lower dimensional face. A partial step is also an in-face step which proposes to stay in the relative interior of the current face. If both of the aforesaid directions fail to meet certain criteria [25], the next iterate takes the regular Frank-Wolfe step, which leads to a further reduction of the computational complexity compared to standard RPCA methods.

Effective utilization of thin SVD is a distinctive attribute of in-face extended Frank-Wolfe algorithm. In a certain iteration q, the thin SVD of C^q is updated and stored

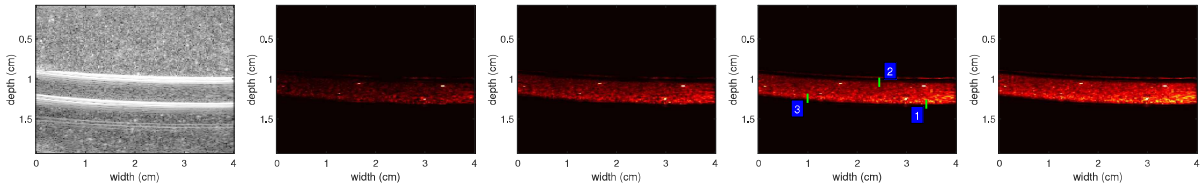

(a) B-mode (b) SVD with $c = 2$, $b = 5$ (c) SVD with $c = 2$, $b = 10$ (d) SVD with $c = 1$, $b = 15$ (e) RAPID

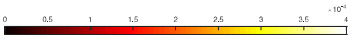

(f) Color bar for conventional data

Figure 3.8: Results for the phantom data with focused conventional imaging. Column 1 shows the B-mode image. Columns 2, 3 and 4 represent the power Doppler images from SVD with different combinations of clutter and blood subspace assumptions. Column 5 depicts the power Doppler image from RAPID. (f) represents the color bar for the power Doppler images.

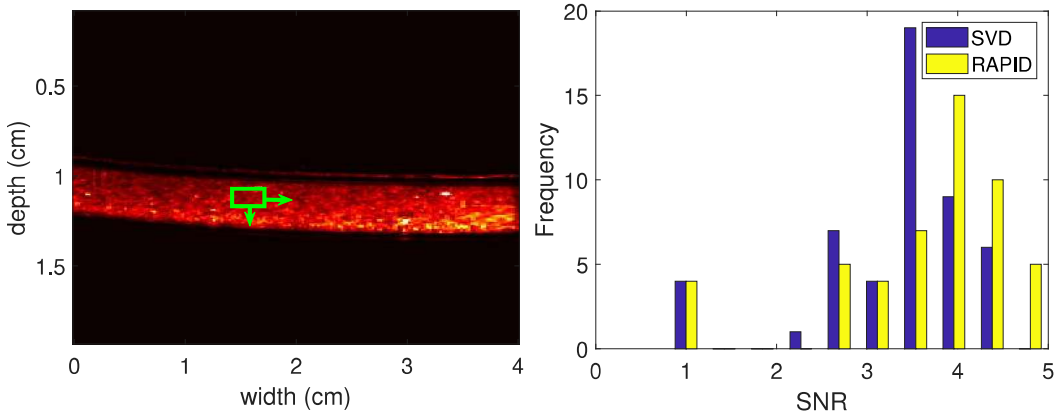

(a) Power Doppler image (b) Histogram of SNR values

Figure 3.9: Histogram of SNR values for the phantom data with focused conventional imaging. SNR values are calculated on 50 different positions of the moving window shown in the left image.

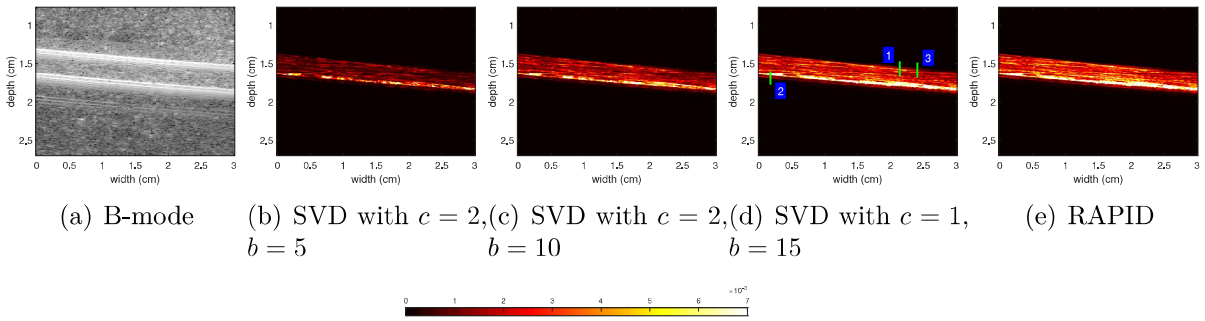

(a) B-mode (b) SVD with $c = 2$, $b = 5$ (c) SVD with $c = 2$, $b = 10$ (d) SVD with $c = 1$, $b = 15$ (e) RAPID

(f) Color bar for plane-wave data

Figure 3.10: Results for the phantom data with plane-wave imaging. Column 1 shows the B-mode image. Columns 2, 3 and 4 represent the power Doppler images from SVD with different combinations of clutter and blood subspace assumptions. Column 5 depicts the power Doppler image from RAPID. (f) represents the color bar for the power Doppler images.

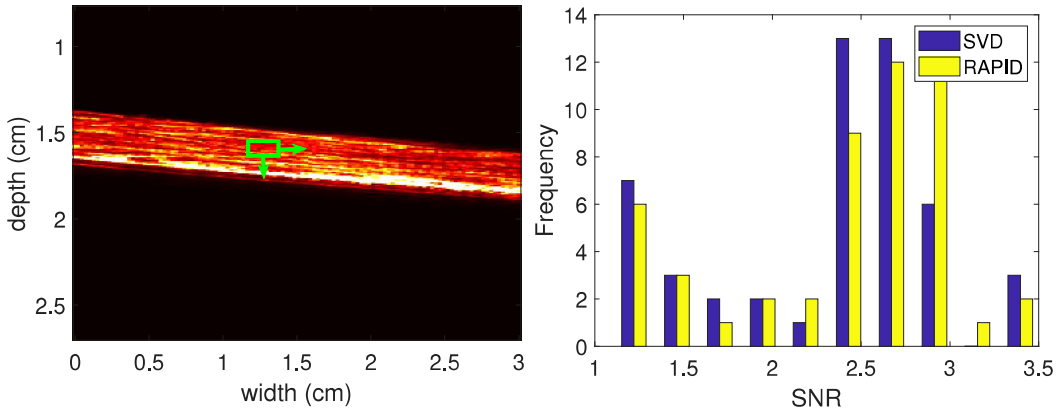

(a) Power Doppler image (b) Histogram of SNR values

Figure 3.11: Histogram of SNR values for the phantom data with plane-wave imaging. SNR values are calculated on 50 different positions of the moving window shown in the left image.

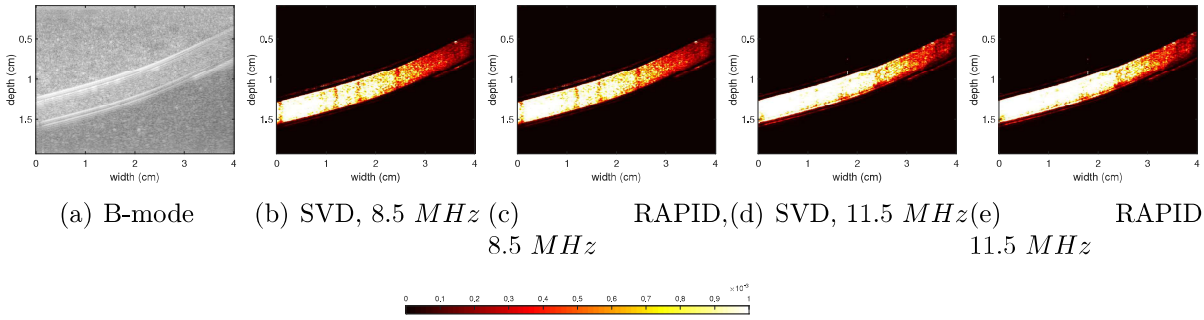

(a) B-mode (b) SVD, 8.5 MHz (c) RAPID,(d) SVD, 11.5 MHz(e) RAPID, 8.5 MHz 11.5 MHz

(f) Color bar

Figure 3.12: Results of the conventional flow phantom experiment for different center frequencies. (a) represents the B-mode image. (b) and (c) show power Doppler images obtained by SVD and RAPID, respectively for 8.5 MHz center frequency. (d) and (e) present power Doppler images from SVD and RAPID, respectively for 11.5 MHz center frequency. (f) shows the color bar for the power Doppler images.

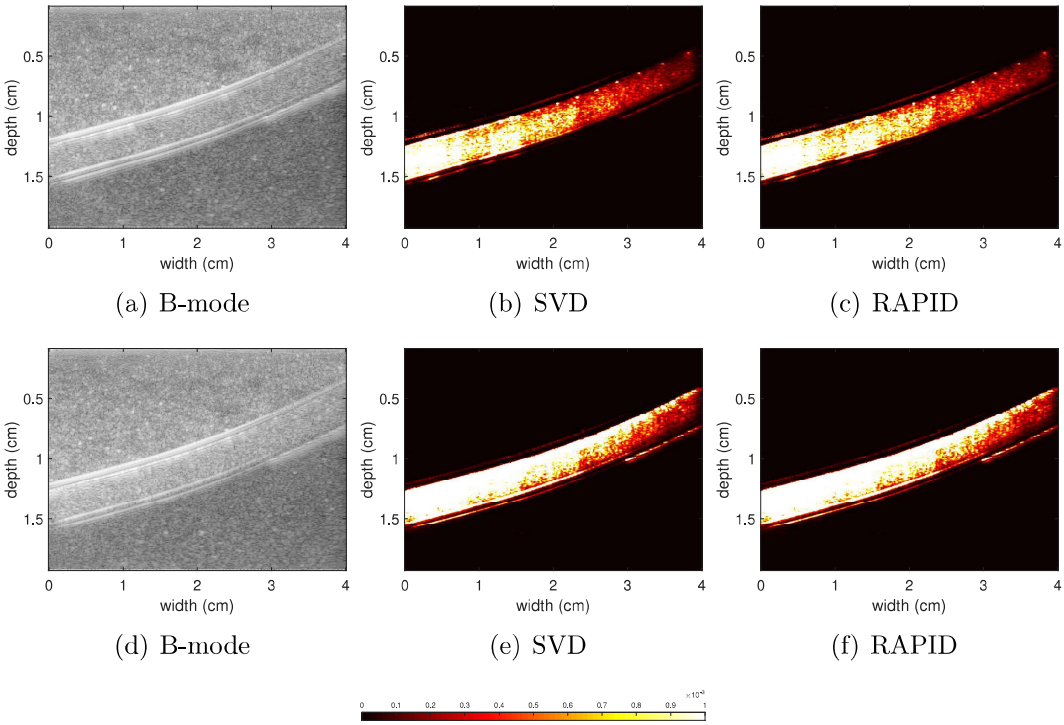

(a) B-mode (b) SVD (c) RAPID

(d) B-mode (e) SVD (f) RAPID

(g) Color bar

Figure 3.13: Results of the conventional flow phantom experiment for different flow rates. Columns 1-3 correspond to B-mode, power Doppler images from SVD and RAPID, respectively. Rows 1 and 2 correspond to slow and fast flows, respectively. (g) represents the color bar for the power Doppler images.

Table 3.1: PSL of the power Doppler images from phantom experiment with conventional imaging. PSL values are calculated on 3 landmarks depicted in Figure 3.8(d).

	SVD	RAPID
Landmark 1	40.79	**41.44**
Landmark 2	61.47	**65.01**
Landmark 3	35.16	**36.57**

Table 3.2: PSL of the power Doppler images from phantom experiment with plane-wave imaging. PSL values are calculated on 3 landmarks depicted in Figure 3.10(d).

	SVD	RAPID
Landmark 1	54.40	**55.25**
Landmark 2	**49.51**	49.42
Landmark 3	61.30	**61.92**

instead of updating C^q. Given the thin SVD of $C^q = U_q \Sigma_q V_q^\dagger$, the number of entries of U_q, Σ_q and $V_q^\dagger$ are mnr^q, r^q and pr^q respectively, where r^q is the rank of C^q. Therefore, while dealing with the thin SVD instead of the full matrix, only $mnr^q + r^q + pr^q$ number of entries are required to be stored. Since C^q corresponds to a low-rank structure in practice, r^q is small. In such a situation, in-face extended Frank-Wolfe method enables us handle a large data matrix with minimal memory consumption.

3.4 Results

We validated the proposed RAPID algorithm using simulation, phantom and *in-vivo* experiments. We used $p = 20$ ultrasound frames in all experiments to generate the clutter suppressed image. We compared our results with the conventional SVD-based technique [22]. Along with qualitative comparison of clutter suppressed power Doppler images, we performed quantitative comparison based on Peak-to-Side Level (PSL) and Signal-to-Noise Ratio (SNR), two conventional quality metrics:

$$\text{PSL} = 20 \log_{10} \left(\frac{\underline{b}}{\underline{c}} \right), \text{SNR} = \frac{\overline{s}}{\sigma} \tag{29}$$

where $\underline{b}$ and $\underline{c}$ denote the peak intensity at the brightest region of the vessel and intensity at the darkest part of the power Doppler image in neighborhood of the peak respectively. $\overline{s}$ and σ stand for the mean and standard deviation of a spatial window located on the vessel.

The codes of SVD and RAPID were implemented in MATLAB and run on a standard 8^{th} generation $3.2GHz$ Intel core-i7 computer. For SVD, we used the MATLAB command "economy SVD", which only calculates and stores the first p left singular vectors for memory and computational efficiency. The runtime of RAPID is similar to that of economy SVD. Therefore, the proposed method is an attractive technique for real-time implementation on commercial ultrasound machines.

3.4.1 Simulation Results

Figure 3.5 depicts the B-mode image along with the clutter suppressed images for the simulation data. The best result from SVD is usually obtained by manually tuning the ranks of clutter and blood subspaces. Power Doppler images generated by SVD with different combinations of clutter and blood ranks are presented in Figure 3.5. Visually, the best clutter suppressed image is obtained by setting the clutter and blood ranks to 1 and 15 respectively, as shown in part (d). No manual tuning is necessary for RAPID to obtain the optimal clutter suppressed image. The proposed technique automatically selects the best combinations of ranks. Figure 3.5 shows that the result from RAPID is qualitatively similar to the best result obtained by SVD. Since both SVD and RAPID fully suppress the background, we did not calculate PSL to avoid infinite quantitative values [82]. We calculated 50 SNR values for different positions of a moving kernel on the blood vessel. We report the histogram of these 50 SNR values in Figure 3.6, which confirms our visual assessment by showing similar SNR values for SVD and RAPID throughout the vessel. The average SNR values corresponding to SVD and RAPID are 2.7174 and 2.7214 respectively. These values are very similar, despite the fact that SVD requires extensive manual intervention to select the boundaries between the subspaces. This, therefore, highlights the quality of our automatic parameter estimation. It is improtant to note that we performed the quantitative comparison between the power Doppler image from RAPID and the best power Doppler image obtained from SVD.

To examine the effect of transmit frequency on clutter rejection, we report the power Doppler images for simulation data collected at three different center frequencies: 7.27 MHz, 8.5 MHz and 10 MHz in Figure 3.7. In all three cases, without requiring any parameter tuning, RAPID's performance is similar to the best performance of SVD. The best vessel enhancement is found at a center frequency of 8.5 MHz for both methods. There are two possible reasons for this. First, since ultrasound images

suffer from lower resolution at lower frequencies, the clutter suppressed images at 8.5 MHz are better than that at 7.27 MHz. Second, although ultrasound images exhibit higher resolution at lower depths in case of high frequencies, the image quality declines beyond a certain depth due to high attenuation of ultrasound waves. Since our simulation frames contain a vessel at a depth of about 1.8 cm, better performance is achieved at 8.5 MHz compared to 10 MHz. Another reason is that the width of our transducer is equal to λ for the 8.5 MHz center frequency, and therefore, optimal results are obtained with both methods at that frequency.

3.4.2 Flow Phantom Results

In the first experiment, conventional focused imaging was performed with a frame rate of 64 fps. Figure 3.8 depicts the clutter rejected images along with the B-mode image. The best result from SVD is selected by manually searching for the best ranks of the clutter and foreground. The result produced by RAPID without requiring any manual tuning (shown in (e)) looks slightly better than the best result from SVD (shown in (d)). Quantitative values of PSL reported in Table 3.1 support our visual assessment. PSL values are calculated on three different landmarks of the power Doppler image indicated in Figure 3.8(d). In addition, we calculated the SNR at 50 different positions of a moving window (see Figure 3.9(a)) on the flow region of the power Doppler image. The SNR values histogram is reported in Figure 3.9(b). The histogram shows that RAPID results in a higher frequency in higher SNR values and lower frequency in lower SNR values. Paired t-test of the SNR values shows that RAPID statistically outperforms SVD with a p-value of 2.75×10^{-18}. This very low p-value is due to the fact that RAPID outperforms SVD throughout the vessel. Furthermore, SVD and RAPID yield average SNR values of 3.31 and 3.62, respectively showing an improvement of 9.35% by RAPID. It is worth mentioning that quantitative comparison is performed between the result from RAPID and the best result obtained from SVD by manually fine-tuning the boundaries between the subspaces.

In the second experiment, plane-wave data with 11.5 MHz center frequency and a scan rate of 565 fps was collected, with all other imaging parameters the same as the conventional beamforming. Figure 3.10 shows the B-mode image, results from SVD for different combinations of clutter and blood ranks and the result from RAPID. Again, RAPID obtains visually superior results compared to SVD by automatically

selecting the optimal clutter-blood boundary. We have reported the PSL values calculated on three different landmarks (see Figure 3.10(d)) in Table 3.2. These quantitative values also demonstrate that RAPID rejects clutter more efficiently than SVD. In Figure 3.11(b), we show the histogram of 50 SNR values calculated at different locations of a moving window (see Figure 3.11(a)). The histogram highlights the fact that RAPID results in a higher frequency at higher SNR values. Furthermore, a paired t-test shows that RAPID statistically outperforms SVD with a p-value of 6.47×10^{-7}. Averaging of the aforementioned 50 SNR values corresponding to SVD and RAPID resulted in mean values of 2.33 and 2.40, respectively. This implies that RAPID provides a 3.02% improvement in SNR over SVD. Similar to the focused phantom experiment, we have reported the quantitative values for the result from RAPID and the best result from SVD.

In the third experiment, we examined the performance of RAPID and SVD on datasets collected at different center frequencies. We conducted a focused flow phantom experiment where RF frames were acquired at 8.5 MHz and 11.5 MHz transmit frequencies. The B-mode and clutter suppressed images are reported in Figure 3.12. In all three cases, RAPID shows similar (if not better) performance as SVD. However, we generate the best results from SVD by extensive manual intervention to select the proper boundaries between subspaces. Best power Doppler images are observed at 11.5 MHz center frequency for both methods. The reason is that the higher frequency image has a good resolution and SNR at shallow depths, where the tube is located.

In the fourth experiment, we investigated the performance of RAPID and SVD with different flow rates by careful mechanical tuning of the flow phantom set-up. We collected RF frames with focused ultrasound imaging from the phantom with flow rates of approximately 1.67 mLs^{-1} (slow flow) and 3.33 mLs^{-1} (fast flow). We show the B-mode and the power Doppler images in Figure 3.13. For both flow rates, RAPID performs slightly better than SVD. SVD shows the best power Doppler images when clutter and blood ranks are manually tuned to 1 and 18, respectively. On the other hand, RAPID obtains the optimal power Doppler images automatically. As expected, both SVD and RAPID obtain their best results for the case of fast flow since the difference between tissue clutter and blood becomes dominant at higher flow velocities.

Table 3.3: PSL of the power Doppler images from the *in-vivo* rat experiment. PSL values are calculated on the 3 landmarks depicted in Figure 3.14(d).

	SVD	RAPID
Landmark 1	34.27	**34.28**
Landmark 2	**39.86**	39.77
Landmark 3	47.81	**47.86**

3.4.3 *in-vivo* Results

Rat Abdomen

B-mode along with the clutter rejected images obtained from SVD and RAPID are reported in Figure 3.14. The abdominal aorta and its branches are not clearly visible in the B-mode image, whereas clutter suppressed power Doppler images reveal the vascular structure very well. We show the power Doppler images obtained from SVD for different combinations of ranks associated with clutter and blood subspaces. The best result is obtained assuming clutter and blood ranks as 1 and 15 respectively (in (d)). Visually, the result from RAPID and the best result obtained from SVD are similar. We performed quantitative comparisons between the best power Doppler image obtained from SVD and the power Doppler image generated by RAPID. The PSL values reported in Table 3.3 show that SVD and RAPID perform almost equally in terms of rejecting clutter. We calculated the PSL values on three landmarks shown in Figure 3.14(d). For a more comprehensive investigation, we calculated the SNR values at 50 different locations of a moving window on the vasculature. The histogram of these 50 SNR values reported in Figure 3.15 shows that the clutter suppression performance of RAPID is similar to that of SVD. Statistical paired t-test provides a p-value of 0.2226, confirming that there is no significant difference in SNR values of power Doppler images obtained from SVD and RAPID. The average of the 50 SNR values corresponding to SVD and RAPID are 0.9138 and 0.9146, respectively, further highlighting the performance similarity between SVD and RAPID.

Human Knee

The conventional beamformed B-mode image as well as the power Doppler images are shown in Figure 3.16. It is evident that suppression of clutter aids clear visualization of the lateral inferior genicular artery and branches coming from fibular and anterior recurrent tibial arteries. Figure 3.16 also shows that the performance of SVD is highly

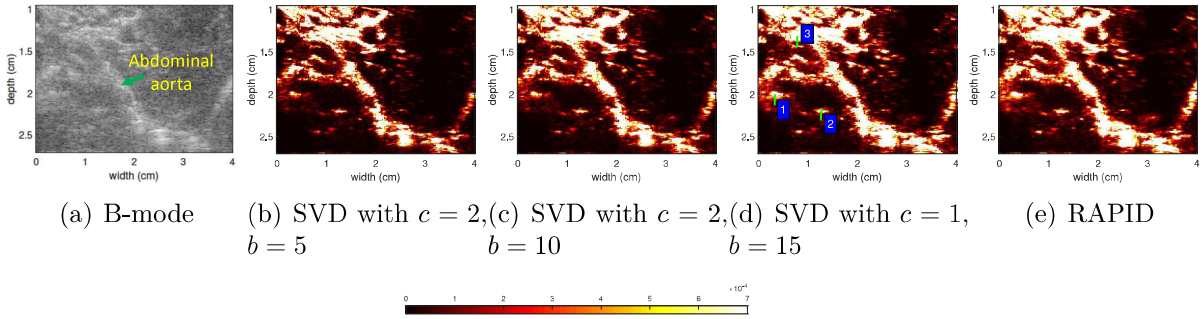

(a) B-mode (b) SVD with $c = 2$, $b = 5$ (c) SVD with $c = 2$, $b = 10$ (d) SVD with $c = 1$, $b = 15$ (e) RAPID

(f) Color bar

Figure 3.14: Results obtained from *in-vivo* data collected from the abdomen of a rat. Column 1 depicts the B-mode image. Columns 2, 3 and 4 show the power Doppler images from SVD with different combinations of clutter and blood subspaces. Column 5 presents the power Doppler image from RAPID. (f) shows the color bar for the power Doppler images.

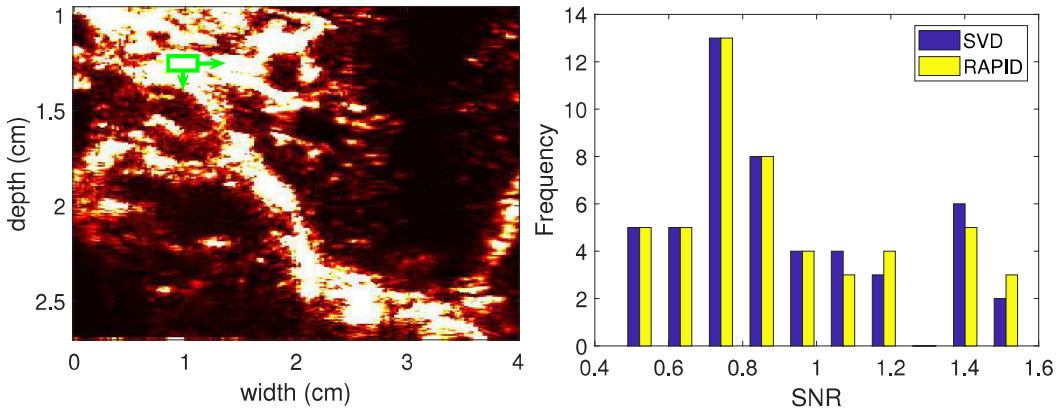

(a) Power Doppler image (b) Histogram of SNR values

Figure 3.15: Histogram of SNR values for the *in-vivo* rat experiment. SNR values are calculated at 50 different locations of the moving window shown in the left image.

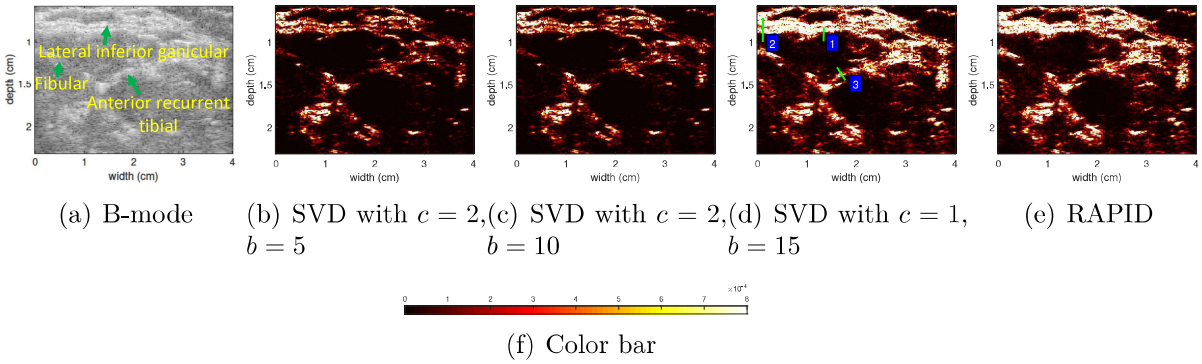

(a) B-mode (b) SVD with $c = 2$, $b = 5$ (c) SVD with $c = 2$, $b = 10$ (d) SVD with $c = 1$, $b = 15$ (e) RAPID

(f) Color bar

Figure 3.16: Results obtained from *in-vivo* data collected from the knee of a human subject. Column 1 depicts the B-mode image. Columns 2, 3 and 4 show the power Doppler images from SVD with different combinations of clutter and blood subspaces. Column 5 presents the power Doppler image from RAPID. (f) shows the color bar for the power Doppler images.

Table 3.4: PSL of the power Doppler images from *in-vivo* human knee experiment. PSL values are calculated on the 3 landmarks shown in Figure 3.16(d).

	SVD	RAPID
Landmark 1	**60.22**	60.2
Landmark 2	47.02	47.02
Landmark 3	33.77	**33.78**

dependent on the selection of ranks associated with clutter and blood subspaces. In this case, SVD shows its best performance when clutter and blood ranks are considered to be 1 and 15, respectively. In contrast, RAPID is capable of generating the most optimal result without any manual tuning. Visual assessment shows that the power Doppler image obtained from RAPID is similar to the best power Doppler image produced by SVD. Similarly to all other experiments, we compared the result of our method to the best result obtained from SVD quantitatively. PSL values reported in Table 3.4 confirm our visual interpretation. In addition, the histogram of 50 SNR values on different locations of a moving window reported in Figure 3.17 also suggests that SVD and RAPID are similarly effective at suppressing clutter. The average SNR values for SVD and RAPID are 0.9440 and 0.9441, respectively, again showing similar performances.

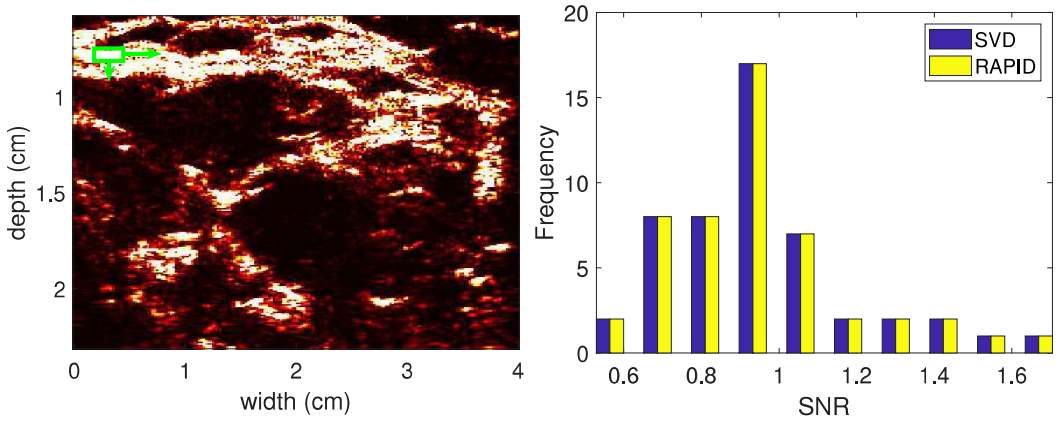

(a) Power Doppler image (b) Histogram of SNR values

Figure 3.17: Histogram of SNR values for the *in-vivo* human knee experiment. SNR values are calculated on 50 different locations of the moving window presented in the left image.

3.5 Discussion

It is evident from the results that the clutter suppression efficiency of SVD is highly dependent on proper selection of the ranks of the subspaces, a process that is currently performed manually. This manual involvement hinders clinical adoption of clutter suppression. On the contrary, RAPID selects the ranks automatically with a guarantee of converging to the optimal solution.

SVD is proven to be a promising technique in ultrasound clutter suppression. However, it fails while dealing with data contaminated with outliers [90]. The robustness of RPCA methods to noise is validated with video data in the field of computer vision. Since RF frames acquired with ultrasound are likely to be noisy, robust matrix decomposition methods can potentially be more advantageous than SVD in ultrasound clutter suppression.

The number of frames used to formulate the data matrix is an important concern. Generally, vessels are better visualized when the number of RF frames is increased as more temporal information is incorporated. However, if the data acquisition rate is low, including more frames leads to a significant increase in signal decorrelation noise which might cause the SVD methods to fail. The optimal number of frames likely depends on the imaging frame-rate and extent of physiological motions in tissue. Selection of the optimal number of frames is an interesting avenue of further research. Here we show that RAPID is capable of obtaining power Doppler images from ultrasound frames collected at different transmit frequencies. However, selection of a

proper center frequency is vital for optimally enhancing the vessel. While looking at the superficial vascular structure, a high frequency ultrasound probe should be used for data acquisition to achieve the best resolution. On the other hand, a lower frequency probe is preferable to collect frames from a deeper vascular network, since high frequency ultrasound waves attenuate faster. When we are interested in a vascular structure at moderate depth, careful tuning of transmit frequency is required to compromise between resolution and penetration depth.

In case of slow blood flow, the task of clutter suppression becomes difficult because slowly flowing blood is hardly distinguishable from the steady tissue clutter. However, our investigation on the flow phantom proves that RAPID is capable of generating high quality power Doppler images for both slow and fast flow rates. Although RAPID does not show large improvement over SVD for different flow rates, RAPID converges to the best attainable result without requiring the manual tuning necessary for SVD.

As the steady background is estimated as a low rank structure in robust matrix decomposition algorithms, high frame to frame correlation is an important requirement. The individual RF frames are stacked in different columns of the data matrix, and as such, should be highly correlated to each other. Therefore, the method could fail in the event of a large out-of-plane movement of the ultrasound probe while collecting the data. Although we did not notice large performance degradation of the proposed RAPID algorithm with possible out-of-plane motion of the probe, 3D data collection from a 2D array can alleviate this problem. Another potential solution to this limitation is introducing a robust image alignment step in every iteration of the RAPID algorithm. The sparsity of the blood component is another important underlying assumption of our algorithm. Although blood is sparser than tissue components in usual scenarios, rapid signal fluctuations caused by turbulent flow in the time domain can affect the spatial sparsity [100]. Imposing the sparsity condition on an appropriate transform (e.g. Fourier Transform) of the blood component instead of the blood component itself might be a promising technique to handle such non-sparsities [100].

3.6 Summary

In this chapter, we proposed RAPID: **R**obust m**A**trix decom**P**osition for suppress**I**ng clutter in ultrasoun**D**, wherein we suggested to enhance blood vessels and suppress unexpected clutter signals by incorporating recently proposed robust matrix completion and optimization algorithms. Validation with simulation, flow phantom and

in-vivo data proved that RAPID does not require any manual intervention required to select the true boundary between blood subspace and clutter, and as such, automates the process of clutter rejection with a guarantee of optimality. RAPID is also computationally efficient and can be implemented in real-time. These features can potentially help ultrasound-based vascular imaging to reach a wider clinical adoption.

Chapter 4

Conclusion and Future Work

4.1 Concluding Remark

Tracking tissue motion is important for numerous medical imaging applications to investigate the physiological condition of the tissue. This motion tracking task can be accomplished by taking advantage of the high data acquisition rate of ultrasound imaging. However, ultrasound motion tracking is an ill-posed problem since the number of unknowns is more than the number of equations. In this thesis, two novel methods are proposed to tackle this problem. In the first method, motion estimation is developed for ultrasound elastography, and in the second method, motion is detected to perform ultrasound clutter suppression for enhancing blood flow.

The method proposed in Chapter 2 of this thesis concerns developing an ultrasound elastography algorithm for tracking tissue motion while undergoing deformation due to internal or external force. This algorithm takes three ultrasound RF frames into consideration and exploits data similarities between pre- and post-deformation frames, as well as spatial and temporal continuities to form a non-linear cost function. This cost function has been optimized efficiently to convert the time delay estimation problem into a sparse system of linear equations with millions of variables. The proposed technique is capable of solving the sparse system for this very large number of variables to find a $2D$ displacement estimate of each sample in a RF frame within a minimal period of time. This unique attribute makes the proposed method suitable for real-time implementation on clinical ultrasound machines. Extensive quantitative and statistical validation with simulation, phantom and *in-vivo* liver cancer data proves the superiority of the proposed technique over the state-of-the-art elastography

techniques. We have made the code associated with this chapter available online to increase the impact of our work.

A novel ultrasound clutter suppression technique has been proposed in Chapter 3 of this thesis. Although the conventional SVD-based methods are successful in suppressing clutter components of ultrasound color flow images, optimality of the result obtained from them is highly dependent on the proper selection of boundaries between different subspaces. This selection is currently performed manually, resulting in two important drawbacks. First, efficient clutter suppression is prone to failure while dealing with a large dataset since it is very difficult to attain the best possible result by manually tuning over a large range. Second, extensive manual trial makes the clutter suppression task very user-dependent, limiting its clinical value. The algorithm proposed in this thesis resolves this well-known issue by casting the clutter suppression problem as a foreground-background separation where clutter is the steady background and blood is considered to be the sparse moving component. The fast Robust Matrix Completion (fRMC) algorithm has been adapted to accomplish this task by utilizing the in-face extended Frank-Wolfe method. This technique makes the clutter rejection problem automatic by eliminating the requirement of manual tuning of the foreground and background dimensions. In addition, this method is efficient in terms of execution time and memory footprint. Simulation, phantom and *in-vivo* animal and human experiments validate that the proposed technique performs as well as the conventional algorithm without requiring any manual tuning.

4.2 Future Work

The technical and clinical aspects of the proposed elastography algorithm, GUEST, can be improved or extended in the future stages of this work. The scopes for technical advancement are listed below:

- Instead of three frames, more RF frames can be incorporated to devise a cost function to investigate if it improves the displacement tracking accuracy. The optimal number of frames needed to balance the quality of the strain image versus computational complexity can also be found from this investigation.
- Although adaptive spatial and temporal regularizations make our algorithm less sensitive to the values of the tunable parameters, a data-driven parameter selection step can be introduced to fully automate the proposed technique.

- In the current version of our work, two initial displacement fields are obtained by running DP twice: once between first and second frames and once between second and third frames. A novel DP framework incorporating three RF frames can be formulated to find two initial displacement estimates simultaneously with better accuracy. In addition, DP over the whole image instead of DP on individual RF lines might also be considered to further improve the initial estimation.

- The proposed algorithm can be extended for working with $3D$ ultrasound frames collected with a $2D$ linear array probe to produce $3D$ strain images with a complete visualization of different types of abnormal tissue such as cyst, benign lesion, tumor etc.

- Deep convolutional neural networks can be utilized in ultrasound elastography [101, 102]. Application of deep learning to ultrasound elastography in spatial and temporal domains is an interesting avenue of future work.

In this thesis, it has been shown that GUEST is capable of improving the visualization of liver tumors through high quality elasticity imaging. In the future, the method can be validated with clinical breast elastography data to examine its ability to characterize breast cancer. In addition, the method can be applied on Breast Cancer Related Lymphedema (BCRL) [103] data to investigate its promise to detect BCRL. Further research might be conducted to check the method's potential to help monitor cardiac and neuro health by strain imaging.

The two proposed techniques are not only novel and valuable on their own, but their combination can also lead to greater clinical usefulness and efficacy. The ultrasound clutter suppression method, RAPID performs well when the data frames are correlated with each other. In case of high temporal decorrelation due to sonographer's hand motion or unexpected movement of the subject, the underlying low rank structure of the data matrix no longer exists. In a future work, frame to frame movement of the background can be estimated by GUEST (the proposed motion estimation algorithm) as a pre-processing step to compensate for the temporal decorrelation so that the data matrix becomes suitable for RAPID by holding a low rank structure. Therefore, this work can be a productive combination of the two motion tracking techniques proposed in this thesis. In addition, an adaptive motion correction step can be embedded in RAPID to align the ultrasound frames and find the low rank

component of the data matrix in a unified framework. Moreover, extensive amount of slow-time temporal frames can be taken into account to assess the effect of number of data samples on clutter suppression efficiency. Furthermore, Convolutional Neural Network (CNN) based background suppression techniques can be adapted to solve ultrasound clutter suppression problem with a better data dependence. Exploring different data types to assure optimal background rejection is an interesting avenue of future research. In this regard, the proposed technique might be extended to work with pre-beamformed ultrasound channel data for obtaining power Doppler images with better resolution since pre-beamformed channel data contains more information than beamformed RF data. Processing a data tensor instead of a data matrix might be considered to increase the clutter suppression efficiency. Besides, complete visualization of blood vessels can be achieved by employing $3D$ ultrasound data in RAPID. To analyze the clinical impact of the proposed theoretic work, RAPID can be tested on *in-vivo* data with vasculature containing plaque or stenosis.

Bibliography

[1] R. E. Davidsen and S. W. Smith, "Two-dimensional arrays for medical ultrasound using multilayer flexible circuit interconnection," *IEEE Transactions on Ultrasonics, Ferroelectrics, and Frequency Control*, vol. 45, no. 2, pp. 338–348, 1998.

[2] F. S. Foster, K. A. Harasiewicz, and M. D. Sherar, "A history of medical and biological imaging with polyvinylidene fluoride (pvdf) transducers," *IEEE Transactions on Ultrasonics, Ferroelectrics, and Frequency Control*, vol. 47, no. 6, pp. 1363–1371, 2000.

[3] P. N. T. Wells, "Ultrasound imaging," *Physics in Medicine Biology*, vol. 51, no. 13, 2006.

[4] R. De Luca, T. Dattoma, L. Forzoni, J. Bamber, P. Palchetti, and A. Gubbini, "Diagnostic ultrasound probes: A typology and overview of technologies," *Current Directions in Biomedical Engineering*, vol. 4, pp. 49–53, 2018.

[5] H. Rivaz, E. M. Boctor, M. A. Choti, and G. D. Hager, "Real-time regularized ultrasound elastography," *IEEE Transactions on Medical Imaging*, vol. 30, no. 4, pp. 928–945, 2011.

[6] H. S. Hashemi and H. Rivaz, "Global time-delay estimation in ultrasound elastography," *IEEE Transactions on Ultrasonics, Ferroelectrics, and Frequency Control*, vol. 64, no. 10, pp. 1625–1636, 2017.

[7] A. Nahiyan and M. K. Hasan, "Hybrid algorithm for elastography to visualize both solid and fluid-filled lesions," *Ultrasound in Medicine & Biology*, vol. 41, no. 4, pp. 1058 – 1078, 2015.

[8] H. G. Kim, M. S. Park, J.-D. Lee, and S. Y. Park, "Ultrasound elastography of the neonatal brain: Preliminary study," *Journal of Ultrasound in Medicine*, vol. 36, no. 7, pp. 1313–1319, 2017.

[9] M. Tanter and M. Fink, "Ultrafast imaging in biomedical ultrasound," *IEEE transactions on ultrasonics, ferroelectrics, and frequency control*, vol. 61, pp. 102–119, 2014.

[10] K. R. Nightingale, M. L. Palmeri, R. W. Nightingale, and G. E. Trahey, "On the feasibility of remote palpation using acoustic radiation force," *The Journal of the Acoustical Society of America*, vol. 110, no. 1, pp. 625–634, 2001.

[11] A. D. Association, "Peripheral arterial disease in people with diabetes," *Diabetes Care*, vol. 26, no. 12, pp. 3333–3341, 2003.

[12] K. Christensen-Jeffries, J. Brown, P. Aljabar, M. Tang, C. Dunsby, and R. J. Eckersley, "3-d in vitroacoustic super-resolution and super-resolved velocity mapping using microbubbles," *IEEE Transactions on Ultrasonics, Ferroelectrics, and Frequency Control*, vol. 64, no. 10, pp. 1478–1486, 2017.

[13] S. C. Uppu, R. Sachdeva, and M. Imamura, "Idiopathic giant right atrial aneurysm," *Ann Pediatr Cardiol*, vol. 6, no. 1, pp. 68 – 70, 2013.

[14] A. Alrifai, M. Kabach, J. Nieves, J. Pino, and R. Chait, "Microvascular coronary artery disease: Review article," *US Cardiology Review*, vol. 12, no. 1, pp. 41–45, 2018.

[15] J. A. Jensen, "Stationary echo cancelling in velocity estimation by time-domain cross-correlation," *IEEE Transactions on Medical Imaging*, vol. 12, no. 3, pp. 471–477, 1993.

[16] A. P. Kadi and T. Loupas, "On the performance of regression and step-initialized iir clutter filters for color doppler systems in diagnostic medical ultrasound," *IEEE Transactions on Ultrasonics, Ferroelectrics, and Frequency Control*, vol. 42, no. 5, pp. 927–937, 1995.

[17] M. E. Allam, R. R. Kinnick, and J. F. Greenleaf, "Isomorphism between pulsed-wave doppler ultrasound and direction-of-arrival estimation. ii. experimental results," *IEEE Transactions on Ultrasonics, Ferroelectrics, and Frequency Control*, vol. 43, no. 5, pp. 923–935, 1996.

[18] J. Bercoff, G. Montaldo, T. Loupas, D. Savery, F. Meziere, M. Fink, and M. Tanter, "Ultrafast compound doppler imaging: providing full blood flow characterization," *IEEE Transactions on Ultrasonics, Ferroelectrics, and Frequency Control*, vol. 58, no. 1, pp. 134–147, 2011.

[19] S. Bjaerum, H. Torp, and K. Kristoffersen, "Clutter filters adapted to tissue motion in ultrasound color flow imaging," *IEEE Transactions on Ultrasonics, Ferroelectrics, and Frequency Control*, vol. 49, no. 6, pp. 693–704, 2002.

[20] P. J. Vaitkus, R. S. C. Cobbold, and K. W. Johnston, "A new time-domain narrowband velocity estimation technique for doppler ultrasound flow imaging. ii. comparative performance assessment," *IEEE Transactions on Ultrasonics, Ferroelectrics, and Frequency Control*, vol. 45, no. 4, pp. 955–971, 1998.

[21] L. A. F. Ledoux, P. Brands, and A. P. G. Hoeks, "Reduction of the clutter component in doppler ultrasound signals based on singular value decomposition: A simulation study," *Ultrasonic imaging*, vol. 19, pp. 1–18, 1997.

[22] C. Demené, T. Deffieux, M. Pernot, B. Osmanski, V. Biran, J. Gennisson, L. Sieu, A. Bergel, S. Franqui, J. Correas, I. Cohen, O. Baud, and M. Tanter, "Spatiotemporal clutter filtering of ultrafast ultrasound data highly increases doppler and fultrasound sensitivity," *IEEE Transactions on Medical Imaging*, vol. 34, no. 11, pp. 2271–2285, 2015.

[23] M. Kim, C. K. Abbey, J. Hedhli, L. W. Dobrucki, and M. F. Insana, "Expanding acquisition and clutter filter dimensions for improved perfusion sensitivity," *IEEE Transactions on Ultrasonics, Ferroelectrics, and Frequency Control*, vol. 64, no. 10, pp. 1429–1438, 2017.

[24] B. Rezaei and S. Ostadabbas, "Background subtraction via fast robust matrix completion," in *Proceedings of the IEEE International Conference on Computer Vision*, pp. 1871–1879, 2017.

[25] P. G. Robert M. Freund and R. Mazumder, "An extended frank-wolfe method with "in-face" directions, and its application to low-rank matrix completion," *SIAM J. Optimization*, vol. 27, no. 1, p. 319–346, 2017.

[26] M. Ashikuzzaman, C. J. Gauthier, and H. Rivaz, "Global ultrasound elastography in spatial and temporal domains," *IEEE Transactions on Ultrasonics, Ferroelectrics, and Frequency Control*, vol. 66, no. 5, pp. 876–887, 2019.

[27] M. Ashikuzzaman, C. Belasso, M. G. Kibria, A. Bergdahl, C. J. Gauthier, and H. Rivaz, "Low rank and sparse decomposition of ultrasound color flow images for suppressing clutter in real time," *IEEE Transactions on Medical Imaging, revision under review*, 2019.

[28] M. Ashikuzzaman, C. Belasso, C. J. Gauthier, and H. Rivaz, "Suppressing clutter components in ultrasound color flow imaging using robust matrix completion algorithm: Simulation and phantom study," in *IEEE International Symposium on Biomedical Imaging (IEEE ISBI)*, 2019.

[29] J. Gennisson, T. Deffieux, M. Fink, and M. Tanter, "Ultrasound elastography: Principles and techniques," *Diagnostic and Interventional Imaging*, vol. 94, no. 5, pp. 487 – 495, 2013.

[30] T. Hall, P. E. Barboneg, A. A. Oberai, J. Jiang, J.-F. Dord, S. Goenezen, and T. Fisher, "Recent results in nonlinear strain and modulus imaging," vol. 7, pp. 313–327, 11 2011.

[31] K. J. Parker, M. M. Doyley, and D. J. Rubens, "Imaging the elastic properties of tissue: the 20 year perspective," *Physics in Medicine & Biology*, vol. 56, no. 1, p. R1, 2011.

[32] J. Ophir, S. K. Alam, B. Garra, F. Kallel, E. Konofagou, T. Krouskop, and T. Varghese, "Elastography: Ultrasonic estimation and imaging of the elastic properties of tissues," *Proceedings of the Institution of Mechanical Engineers, Part H: Journal of Engineering in Medicine*, vol. 213, no. 3, pp. 203–233, 1999.

[33] G. Treece, J. Lindop, L. Chen, J. Housden, R. Prager, and A. Gee, "Real-time quasi-static ultrasound elastography," vol. 1, pp. 540–52, 08 2011.

[34] M. Omidyeganeh, Y. Xiao, M. O. Ahmad, and H. Rivaz, "Estimation of strain elastography from ultrasound radio-frequency data by utilizing analytic gradient of the similarity metric," *IEEE Transactions on Medical Imaging*, vol. 36, no. 6, pp. 1347–1358, 2017.

[35] K. M. Hiltawsky, M. Krüger, C. Starke, L. Heuser, H. Ermert, and A. Jensen, "Freehand ultrasound elastography of breast lesions: clinical results," *Ultrasound in Medicine & Biology*, vol. 27, no. 11, pp. 1461 – 1469, 2001.

[36] M. Yamakawa, N. Nitta, T. Shiina, T. Matsumura, S. Tamano, T. Mitake, and E. Ueno, "High-speed freehand tissue elasticity imaging for breast diagnosis," vol. 42, pp. 3265–3270, 05 2003.

[37] E. Turgay, S. Salcudean, and R. Rohling, "Identifying the mechanical properties of tissue by ultrasound strain imaging," *Ultrasound in Medicine & Biology*, vol. 32, no. 2, pp. 221 – 235, 2006.

[38] A. Basarab, A. Lyshchik, and P. Delachartre, "Multi-frame motion estimation for freehand elastography and its application to thyroid tumor imaging," in *2008 5th IEEE International Symposium on Biomedical Imaging: From Nano to Macro*, pp. 532–535, 2008.

[39] X. Pan, K. Liu, J. Bai, and J. Luo, "A regularization-free elasticity reconstruction method for ultrasound elastography with freehand scan," *BioMedical Engineering OnLine*, vol. 13, p. 132, Sep 2014.

[40] M. G. Kibria and M. K. Hasan, "A class of kernel based real-time elastography algorithms," *Ultrasonics*, vol. 61, pp. 88 – 102, 2015.

[41] X. Pan, K. Liu, J. Shao, J. Gao, L. Huang, J. Bai, and J. Luo, "Performance comparison of rigid and affine models for motion estimation using ultrasound radio-frequency signals," *IEEE Transactions on Ultrasonics, Ferroelectrics, and Frequency Control*, vol. 62, no. 11, pp. 1928–1943, 2015.

[42] J. Wang, Q. Huang, and X. Zhang, "Ultrasound elastography based on the normalized cross-correlation and the pso algorithm," pp. 1131–1135, 11 2017.

[43] L. Yuan and P. C. Pedersen, "Analytical phase-tracking-based strain estimation for ultrasound elasticity," *IEEE Transactions on Ultrasonics, Ferroelectrics, and Frequency Control*, vol. 62, no. 1, pp. 185–207, 2015.

[44] H. Rivaz, E. Boctor, P. Foroughi, R. Zellars, G. Fichtinger, and G. Hager, "Ultrasound elastography: A dynamic programming approach," *IEEE Transactions on Medical Imaging*, vol. 27, no. 10, pp. 1373–1377, 2008.

[45] C. Pellot-Barakat, F. Frouin, M. F. Insana, and A. Herment, "Ultrasound elastography based on multiscale estimations of regularized displacement fields," *IEEE Transactions on Medical Imaging*, vol. 23, no. 2, pp. 153–163, 2004.

[46] J. Jiang and T. J. Hall, "A generalized speckle tracking algorithm for ultrasonic strain imaging using dynamic programming," *Ultrasound in Medicine & Biology*, vol. 35, no. 11, pp. 1863 – 1879, 2009.

[47] H. Rivaz, E. M. Boctor, M. A. Choti, and G. D. Hager, "Ultrasound elastography using multiple images," *Medical Image Analysis*, vol. 18, no. 2, pp. 314 – 329, 2014.

[48] R. Zahiri-Azar and S. E. Salcudean, "Motion estimation in ultrasound images using time domain cross correlation with prior estimates," *IEEE Trans. Biomedical Engineering*, vol. 53, no. 10, pp. 1990–2000, 2006.

[49] A. Kuzmin, A. M. Zakrzewski, B. W. Anthony, and V. Lempitsky, "Multiframe elastography using a handheld force-controlled ultrasound probe," *IEEE Transactions on Ultrasonics, Ferroelectrics, and Frequency Control*, vol. 62, pp. 1486–1500, August 2015.

[50] A. Ramalli, O. Basset, C. Cachard, E. Boni, and P. Tortoli, "Frequency-domain-based strain estimation and high-frame-rate imaging for quasi-static elastography," *IEEE Transactions on Ultrasonics, Ferroelectrics, and Frequency Control*, vol. 59, no. 4, pp. 817–824, 2012.

[51] F. Viola and W. F. Walker, "A comparison of the performance of time-delay estimators in medical ultrasound," *IEEE Transactions on Ultrasonics, Ferroelectrics, and Frequency Control*, vol. 50, no. 4, pp. 392–401, 2003.

[52] S. R. Ara, F. Mohsin, F. Alam, S. A. Rupa, S. Y. Lee, M. K. Hasan, and R. Awwal, "Phase-based direct average strain estimation for elastography," *IEEE Transactions on Ultrasonics, Ferroelectrics, and Frequency Control*, vol. 60, no. 11, pp. 2266–2283, 2013.

[53] H. Hasegawa and H. Kanai, "Improving accuracy in estimation of artery-wall displacement by referring to center frequency of rf echo," *IEEE Transactions on Ultrasonics, Ferroelectrics, and Frequency Control*, vol. 53, no. 1, pp. 52–63, 2006.

[54] J. Grondin, E. Wan, A. Gambhir, H. Garan, and E. E. Konofagou, "Intracardiac myocardial elastography in canines and humans in vivo," *IEEE Transactions on Ultrasonics, Ferroelectrics, and Frequency Control*, vol. 62, no. 2, pp. 337–349, 2015.

[55] W. F. Walker and G. E. Trahey, "A fundamental limit on delay estimation using partially correlated speckle signals," *IEEE Transactions on Ultrasonics, Ferroelectrics, and Frequency Control*, vol. 42, no. 2, pp. 301–308, 1995.

[56] M. O'Donnell, A. R. Skovoroda, B. M. Shapo, and S. Y. Emelianov, "Internal displacement and strain imaging using ultrasonic speckle tracking," *IEEE Transactions on Ultrasonics, Ferroelectrics, and Frequency Control*, vol. 41, no. 3, pp. 314–325, 1994.

[57] R. Dickinson and C. Hill, "Measurement of soft tissue motion using correlation between a-scans," *Ultrasound in Medicine & Biology*, vol. 8, no. 3, pp. 263 – 271, 1982.

[58] M. Bilgen and M. Insana, "Deformation models and correlation analysis in elastography," vol. 99, pp. 3212–24, 06 1996.

[59] E. S. Ebbini, "Phase-coupled two-dimensional speckle tracking algorithm," *IEEE Transactions on Ultrasonics, Ferroelectrics, and Frequency Control*, vol. 53, no. 5, pp. 972–990, 2006.

[60] G. M. Treece, J. E. Lindop, A. H. Gee, and R. W. Prager, "Freehand ultrasound elastography with a 3-d probe," *Ultrasound in Medicine & Biology*, vol. 34, no. 3, pp. 463 – 474, 2008.

[61] B. H. Friemel, L. N. Bohs, and G. E. Trahey, "Relative performance of two-dimensional speckle-tracking techniques: normalized correlation, non-normalized correlation and sum-absolute-difference," in *1995 IEEE Ultrasonics Symposium. Proceedings. An International Symposium*, vol. 2, pp. 1481–1484 vol.2, 1995.

[62] E. Brusseau, J. Kybic, J. F. Deprez, and O. Basset, "2-d locally regularized tissue strain estimation from radio-frequency ultrasound images: Theoretical developments and results on experimental data," *IEEE Transactions on Medical Imaging*, vol. 27, no. 2, pp. 145–160, 2008.

[63] J. Jensen, "Field: A program for simulating ultrasound systems," *Medical and Biological Engineering and Computing*, vol. 34, pp. 351–352, 1996.

[64] N. C. Dolan, K. Liu, M. H. Criqui, P. Greenland, J. M. Guralnik, C. Chan, J. R. Schneider, A. L. Mandapat, G. Martin, and M. M. McDermott, "Peripheral artery disease, diabetes, and reduced lower extremity functioning," *Diabetes Care*, vol. 25, no. 1, pp. 113–120, 2002.

[65] R. Zatz and B. M. Brenner, "Pathogenesis of diabetic microangiopathy. the hemodynamic view," *Am. J. Med.*, vol. 80, no. 3, pp. 443–453, 1986.

[66] P. G. Camici and F. Crea, "Coronary microvascular dysfunction," *New Eng. J. Med.*, vol. 356, no. 8, pp. 830–840, 2007.

[67] M. A. Marinescu, A. I. Löffler, M. Ouellette, L. Smith, C. M. Kramer, and J. M. Bourque, "Coronary microvascular dysfunction, microvascular angina, and treatment strategies," *JACC: Cardiovascular Imaging*, vol. 8, no. 2, pp. 210 – 220, 2015.

[68] G. Zoffoli, D. Mangino, A. Venturini, A. Terrini, A. Asta, C. Zanchettin, and E. Polesel, "Diagnosing left ventricular aneurysm from pseudo-aneurysm: a case report and a review in literature," *J Cardiothorac Surg.*, vol. 4, no. 11, 2009.

[69] J. Cronenwett, T. F Murphy, G. B Zelenock, W. Whitehouse, S. M Lindenauer, L. M Graham, L. E Quint, T. M Silver, and J. Caridi, "Actuarial analysis of variables associated with rupture of small abdominal aortic aneurysms," *Surgery*, vol. 98, no. 3, pp. 472 – 483, 1985.

[70] S. Juvela, M. Porras, and K. Poussa, "Natural history of unruptured intracranial aneurysms: probability of and risk factors for aneurysm rupture," *J. Neurosurgery*, vol. 108, no. 5, pp. 1052 – 1060, 2008.

[71] S. Currie, K. Mankad, and A. Goddard, "Endovascular treatment of intracranial aneurysms: review of current practice," *Postgrad Med J*, vol. 87, no. 1023, pp. 41 – 50, 2011.

[72] K. Christensen-Jeffries, R. J. Browning, M.-X. Tang, C. Dunsby, and R. J. Eckersley, "In vivo acoustic super-resolution and super-resolved velocity mapping using microbubbles," *IEEE Transactions on Medical Imaging*, vol. 34, no. 2, pp. 433–440, 2015.

[73] P. Carmeliet and R. K. Jain, "Angiogenesis in cancer and other diseases," *Nature*, vol. 407, no. 6801, pp. 249 – 257, 2000.

[74] N. Nishida, H. Yano, T. Nishida, T. Kamura, and M. Kojiro, "Angiogenesis in cancer," *Vascular Health and Risk Management*, vol. 2, no. 3, pp. 213 – 219, 2006.

[75] S. Bjaerum, H. Torp, and K. Kristoffersen, "Clutter filter design for ultrasound color flow imaging," *IEEE Transactions on Ultrasonics, Ferroelectrics, and Frequency Control*, vol. 49, no. 2, pp. 204–216, 2002.

[76] A. C. H. Yu and L. Lovstakken, "Eigen-based clutter filter design for ultrasound color flow imaging: A review," *IEEE Transactions on Ultrasonics, Ferroelectrics, and Frequency Control*, vol. 57, no. 5, pp. 1096–1111, 2010.

[77] C. Tysoe and D. H. Evans, "Bias in mean frequency estimation of doppler signals due to wall clutter filters," *Ultrasound in Med. & Biol.*, vol. 21, no. 5, pp. 671–677, 1995.

[78] Y. M. Yoo, R. Managuli, and Y. Kim, "Adaptive clutter filtering for ultrasound color flow imaging," *Ultrasound in Med. & Biol.*, vol. 29, no. 9, pp. 1311–1320, 2003.

[79] A. P. G. Hoeks, J. J. W. van de Vorst, A. Dabekaussen, P. J. Brands, and R. S. Reneman, "An efficient algorithm to remove low frequency doppler signals in digital doppler systems," *Ultrasonic Imaging*, vol. 13, pp. 135–144, 1991.

[80] E. Mace, G. Montaldo, I. Cohen, M. Baulac, M. Fink, and M. Tanter, "Functional ultrasound imaging of the brain," *Nature Methods*, vol. 8, pp. 662–664, 2011.

[81] E. J. Candes, C. A. Sing-Long, and J. D. Trzasko, "Unbiased risk estimates for singular value thresholding and spectral estimators," *IEEE Transactions on Signal Processing*, vol. 61, no. 19, pp. 4643–4657, 2013.

[82] M. Bayat, M. Fatemi, and A. Alizad, "Background removal and vessel filtering of noncontrast ultrasound images of microvasculature," *IEEE Transactions on Biomedical Engineering*, vol. 66, no. 3, pp. 831–842, 2019.

[83] S. Adabi, S. Ghavami, M. Fatemi, and A. Alizad, "Non-local based denoising framework for in vivo contrast-free ultrasound microvessel imaging," *Sensors*, vol. 19, 2019.

[84] I. Özdemir and K. Hoyt, "Morphological processing for multiscale analysis of super-resolution ultrasound images of tissue microvascular networks," in *SPIE Medical Imaging*, 2019.

[85] R. Nayak, V. Kumar, J. Webb, A. Gregory, M. Fatemi, and A. Alizad, "Non-contrast agent based small vessel imaging of human thyroid using motion corrected power doppler imaging," *Scientific Reports*, vol. 8, 2018.

[86] M. Kim, Y. Zhu, J. Hedhli, L. W. Dobrucki, and M. F. Insana, "Multidimensional clutter filter optimization for ultrasonic perfusion imaging," *IEEE Transactions on Ultrasonics, Ferroelectrics, and Frequency Control*, vol. 65, no. 11, pp. 2020–2029, 2018.

[87] G. G. Olleros, M. B. Stuart, J. A. Jensen, C. A. Villagómez Hoyos, and K. L. Hansen, "Spatiotemporal filtering for synthetic aperture slow flow imaging," in *IEEE IUS*, pp. 1–4, 2018.

[88] G. Bergqvist and E. G. Larsson, "The higher-order singular value decomposition: Theory and an application [lecture notes]," *IEEE Signal Processing Magazine*, vol. 27, no. 3, pp. 151–154, 2010.

[89] J. Baranger, B. Arnal, F. Perren, O. Baud, M. Tanter, and C. Demené, "Adaptive spatiotemporal svd clutter filtering for ultrafast doppler imaging using similarity of spatial singular vectors," *IEEE Transactions on Medical Imaging*, vol. 37, no. 7, pp. 1574–1586, 2018.

[90] E. J. Candes, X. Li, Y. Ma, and J. Wright, "Robust principal component analysis?," *Journal of the ACM*, vol. 58, no. 3, 2011.

[91] J.-F. Cai, E. J. Candes, and Z. Shen, "A singular value thresholding algorithm for matrix completion," *SIAM J. Optim.*, vol. 20, no. 4, 2010.

[92] V. Chandrasekaran, S. Sanghavi, P. A. Parrilo, and A. S. Willsky, "Rank-sparsity incoherence for matrix decomposition," *SIAM J. Optim.*, vol. 21, no. 2, pp. 572–596, 2011.

[93] J. Wright and Y. Ma, "Dense error correction via ℓ^1-minimization," *IEEE Trans. Information Theory*, vol. 56, no. 7, pp. 3540–3560, 2010.

[94] H. Zhang, W. He, L. Zhang, H. Shen, and Q. Yuan, "Hyperspectral image restoration using low-rank matrix recovery," *IEEE Transactions on Geoscience and Remote Sensing*, vol. 52, no. 8, pp. 4729–4743, 2014.

[95] P. Favaro, R. Vidal, and A. Ravichandran, "A closed form solution to robust subspace estimation and clustering," in *CVPR 2011*, pp. 1801–1807, 2011.

[96] H. Mansour and A. Vetro, "Video background subtraction using semi-supervised robust matrix completion," in *2014 IEEE International Conference on Acoustics, Speech and Signal Processing (ICASSP)*, pp. 6528–6532, 2014.

[97] J. L. Kendall and J. P. Faragher, "Ultrasound-guided central venous access: a homemade phantom for simulation," *Canadian Journal of Emergency Medicine*, vol. 9, no. 5, p. 371–373, 2007.

[98] J. Jensen and N. B. Svendsen, "Calculation of pressure fields from arbitrarily shaped, apodized, and excited ultrasound transducers," *IEEE Transactions on Ultrasonics, Ferroelectrics, and Frequency Control*, vol. 39, pp. 262–267, 1992.

[99] X. Peng, C. Lu, Z. Yi, and H. Tang, "Connections between nuclear-norm and frobenius-norm-based representations," *IEEE Transactions on Neural Networks and Learning Systems*, vol. 29, no. 1, pp. 218–224, 2018.

[100] M. Bayat and M. Fatemi, "Concurrent clutter and noise suppression via low rank plus sparse optimization for non-contrast ultrasound flow doppler processing in microvasculature," in *IEEE International Conference on Acoustics, Speech and Signal Processing (ICASSP)*, pp. 1080–1084, 2018.

[101] M. G. Kibria and H. Rivaz, "Global ultrasound elastography using convolutional neural network," *arXiv preprint arXiv:1805.07493*, 2018.

[102] M. G. Kibria and H. Rivaz, "Gluenet: Ultrasound elastography using convolutional neural network," *Simulation, Image Processing, and Ultrasound Systems for Assisted Diagnosis and Navigation. Springer, Cham*, pp. 21–28, 2018.

[103] H. S. Hashemi, S. Fallone, M. Boily, A. Towers, R. D. Kilgour, and H. Rivaz, "Assessment of mechanical properties of tissue in breast cancer-related lymphedema using ultrasound elastography," *IEEE Transactions on Ultrasonics, Ferroelectrics, and Frequency Control*, vol. 66, no. 3, pp. 541–550, 2019.

Appendix A

Supplementary Material for GUEST

Figure A.1 presents the strain images from GUEST for a simulation phantom with frame to frame strains 0.5% and 3%. For both simulations, regularization parameters were kept the same (α_1=5, α_2=1, α_3=20, β_1=5, β_2=1 and β_3=20). Optimal results for both cases were obtained using the aforesaid parameter settings. This proves that parameter values do not depend on strain percentage which in turn says that parameter values are unrelated to the rate of ultrasound data acquisition.

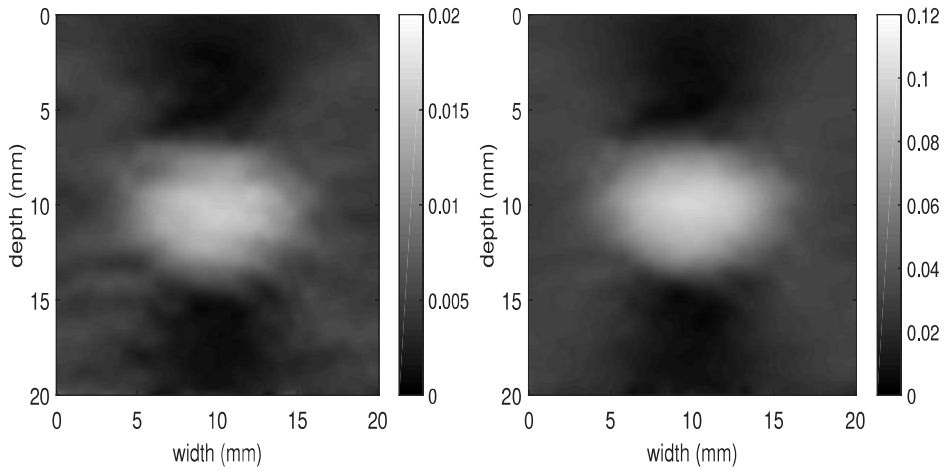

Figure A.1: Axial strain images from GUEST for the simulation phantom with different strain level. First and second columns correspond to the axial strain images for frame to frame strains of 0.5% and 3% respectively.

Figure A.2 shows the strain images and histograms of CNR values for a simulation

phantom with frame to frame strain of 1%, 2% and 3%. In Figure A.2(c), sliding blue target and red background windows for calculating 120 (6 target and 20 background windows) CNR values are shown. Histograms with 120 CNR values are also presented in Figure A.2. Both visual assessment and histograms suggest that GUEST produces better strain images than GLUE and the Hybrid method.

We have simulated a situation where Radio-Frequency (RF) frames are temporally irregular. The strain from first frame to second frame is 0.5% and second frame to third frame is 0.6%. Figure A.3 depicts that GUEST is successful in obtaining a correct strain map even for this temporally discontinuous case. This experiment supports our claim that GUEST is robust to temporal irregularity induced from sinusoidal hand motion or other sources.

We have simulated a homogeneous phantom with an elasticity of 20 kPa using Field II. The simulated phantom contains a hard inclusion with intra-varying elasticity levels of 40 kPa and 80 kPa. We have compressed the phantom using closed form equations. Let us consider the axial and lateral positions of a particular scatterer are z_p and x_p. Lateral displacement of the scatterer is given by:

$$d_x(x_p) = \begin{cases} \nu s_1 x_p & \text{if } z_p \leq D_1 \\ \nu s_2 x_p & \text{if } D_1 < z_p \leq D_2 \\ \nu s_3 x_p & \text{if } D_2 < z_p \leq D_3 \\ \nu s_1 x_p & \text{otherwise} \end{cases} \tag{30}$$

Here, ν is poisson's ratio which is considered to be 0.49 for this experiment. s_1 stands for the percent axial strain in background. s_2 and s_3 are percent strains in the portions of the hard inclusion with elasticities 40 kPa and 80 kPa respectively. $D_1 < z_p \leq D_2$ corresponds to the axial positions with an elasticity of 40 kPa. Similarly, $D_2 < z_p \leq D_3$ is the depth of the tissue with an elasticity of 80 kPa. Axial shift of the scatterer is given by Eq. 31.

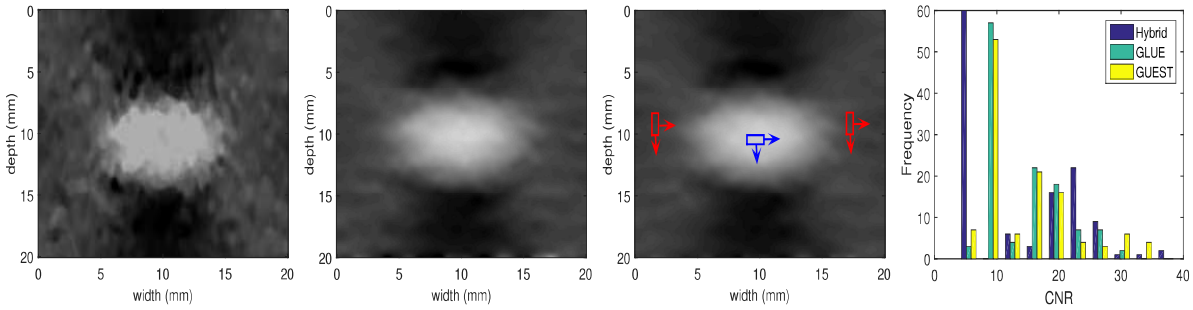

(a) Hybrid for 1% strain (b) GLUE for 1% strain (c) GUEST for 1% strain (d) Histogram of CNR values

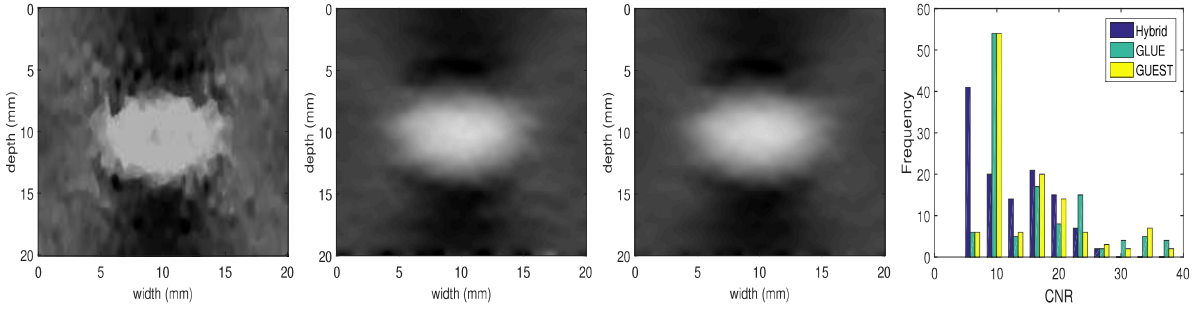

(e) Hybrid for 2% strain (f) GLUE for 2% strain (g) GUEST for 2% strain (h) Histogram of CNR values

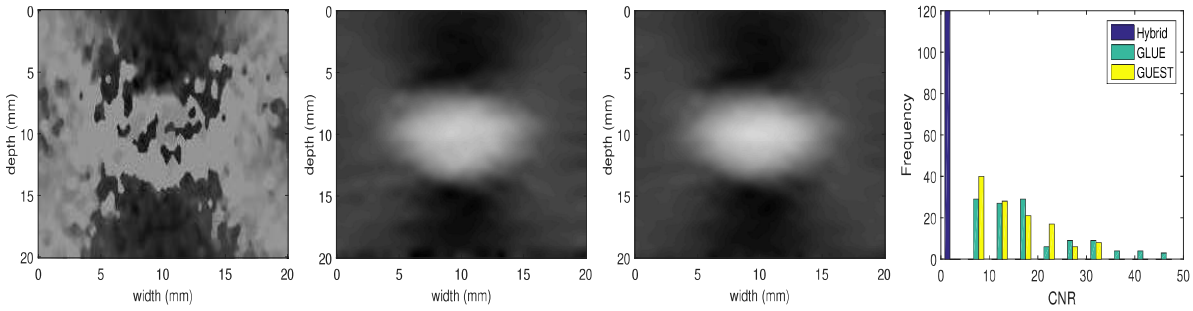

(i) Hybrid for 3% strain (j) GLUE for 3% strain (k) GUEST for 3% strain (l) Histogram of CNR values

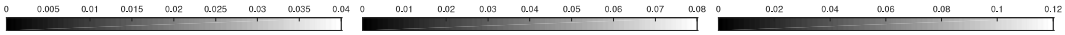

(m) Color bar for 1% strain (n) Color bar for 2% strain (o) Color bar for 3% strain

Figure A.2: Axial strain images and histograms for the simulation phantom. Rows 1, 2 and 3 correspond to frame to frame strain levels of 1%, 2% and 3% respectively. Columns 1-3 show strain images for Hybrid, GLUE and GUEST respectively. Column 4 presents the histograms of CNR values. (m), (n) and (o) correspond to color bars for 1%, 2% and 3% strains respectively.

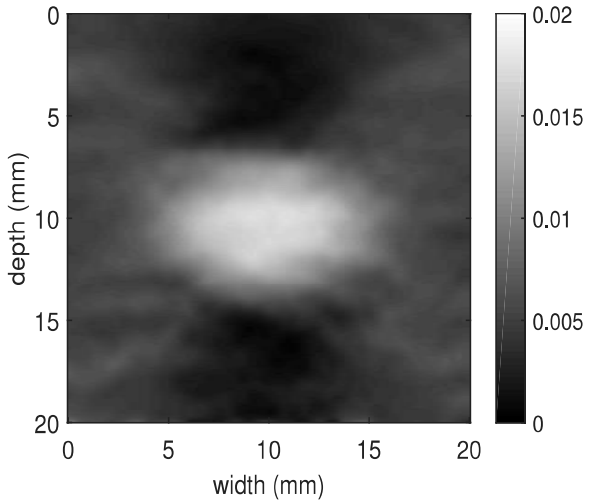

Figure A.3: Axial strain image from GUEST for the simulation phantom with temporal discontinuity.

$$d_z(z_p) = \begin{cases} -s_1 z_p & \text{if } z_p \leq D_1 \\ -s_2(z_p - D_1) - s_1 D_1 & \text{if } D_1 < z_p \leq D_2 \\ -s_3(z_p - D_2) - s_2(D_2 - D_1) - s_1 D_1 & \text{if } D_2 < z_p \leq D_3 \\ -s_1(z_p - D_3) - s_3(D_3 - D_2) - s_2(D_2 - D_1) - s_1 D_1 & \text{otherwise} \end{cases} \tag{31}$$

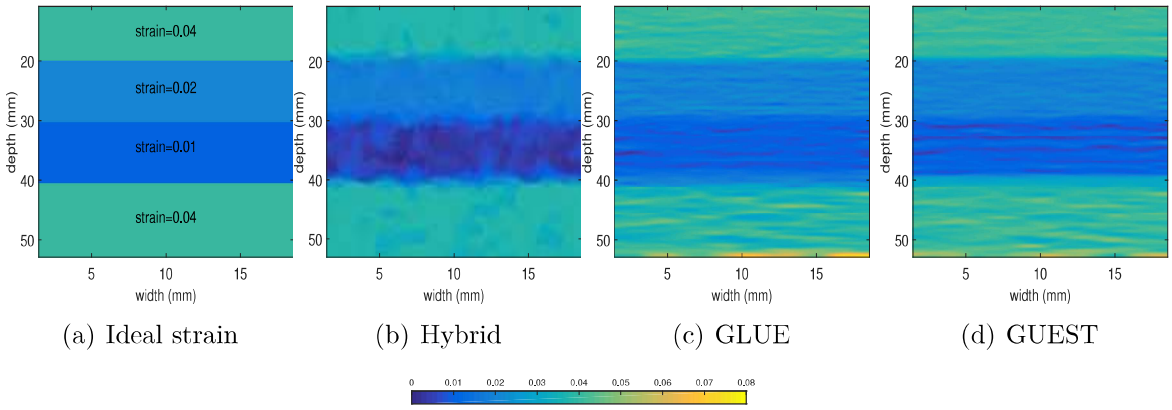

(a) Ideal strain (b) Hybrid (c) GLUE (d) GUEST

(e) Color bar

Figure A.4: Axial strain images for a simulation phantom with an inclusion containing intra-variation in elasticity. Column 1 represents the ideal strain image. Columns 2-4 show strain images for Hybrid, GLUE and GUEST respectively. (e) represents the color bar.

Table A.1: SSIM and PSNR of the strain images for simulation phantom with an inclusion with intra-variation in elasticity.

	SSIM	PSNR (dB)
Hybrid	0.7280	45.7951
GLUE	0.9479	46.6852
GUEST	**0.9509**	**46.8747**

In this experiment, s_1 is considered to be 4%. To comment on s_2 and s_3, let's revisit two basic physics concepts. First, Hooke's law: $\sigma = sE$. Here, σ, s and E correspond to stress, strain and elasticity of a portion of the tissue. Second, equilibrium which means that stresses in different portions of the tissue are equal. In light of these two basic rules, s_2 and s_3 turn out to be 2% and 1% respectively. The ideal and estimated axial strain images from Hybrid, GLUE and GUEST for the simulated phantom are presented in Figure A.4. It is visually clear that the strain image from GUEST shows the boundaries of different layers better than Hybrid and GLUE. Quantitative values of Peak-Signal-to-Noise Ratio (PSNR) and Structural Similarity Index (SSIM) are reported in Table A.1. GUEST provides the highest values for both of the metrics. This particular experiment proves that our method does not over-smooth the strain image. Instead, GUEST better depicts different layers of the tissue than the existing methods.

In Figure A.5, we have presented axial strain images from GUEST for simulation phantom with different sets of parameter values. We have reported results for $\alpha_1 =$

$\beta_1 = 0, 1, 2, 5$. For all four cases of α_1 and β_1, α_2 and β_2 are kept constant at 1 while α_3 and β_3 are set to 20. Additionally, we report results for $\alpha_2 = \beta_2 = 0, 0.1, 0.5, 1$ setting α_1, β_1, α_3 and β_3 to $5, 5, 20$ and 20 respectively. Finally, we have presented axial strain images for $\alpha_3 = \beta_3 = 0, 1, 5, 20$ while α_1, β_1, α_2 and β_2 remain fixed at $5, 5, 1$ and 1 respectively. This experiment shows the dependence of strain estimation on different regularization parameters. Figure A.6 shows the strain profiles from Hybrid, GLUE and GUEST for the simulation data over a vertical cut. GUEST generates a smoother strain profile in uniform regions compared to both GLUE and the Hybrid methods. The strain plot from Hybrid suffers from a large fluctuation of background strain. The diameter of the inclusion is marked with ticks in the x-axis of the strain profile figure.

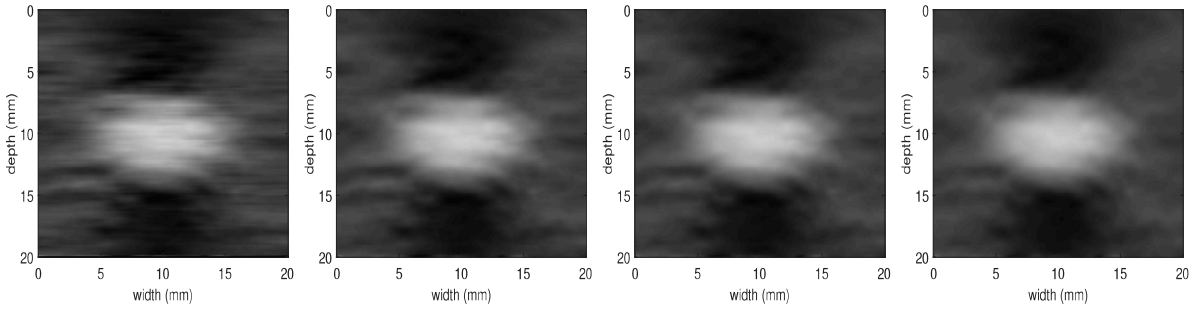

(a) $\alpha_1 = \beta_1 = 0$, $\alpha_2 = \beta_2 = 1$, $\alpha_3 = \beta_3 = 20$ (b) $\alpha_1 = \beta_1 = 1$, $\alpha_2 = \beta_2 = 1$, $\alpha_3 = \beta_3 = 20$ (c) $\alpha_1 = \beta_1 = 2$, $\alpha_2 = \beta_2 = 1$, $\alpha_3 = \beta_3 = 20$ (d) $\alpha_1 = \beta_1 = 5$, $\alpha_2 = \beta_2 = 1$, $\alpha_3 = \beta_3 = 20$

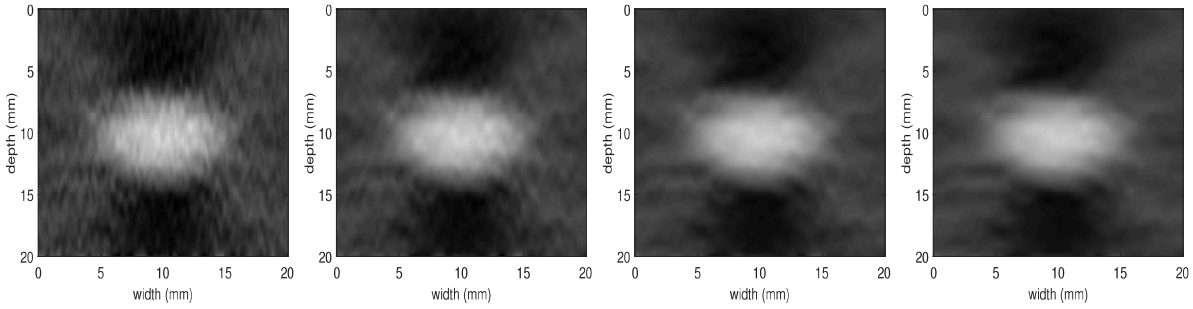

(e) $\alpha_1 = \beta_1 = 5$, $\alpha_2 = \beta_2 = 0$, $\alpha_3 = \beta_3 = 20$ (f) $\alpha_1 = \beta_1 = 5$, $\alpha_2 = \beta_2 = 0.1$, $\alpha_3 = \beta_3 = 20$ (g) $\alpha_1 = \beta_1 = 5$, $\alpha_2 = \beta_2 = 0.5$, $\alpha_3 = \beta_3 = 20$ (h) $\alpha_1 = \beta_1 = 5$, $\alpha_2 = \beta_2 = 1$, $\alpha_3 = \beta_3 = 20$

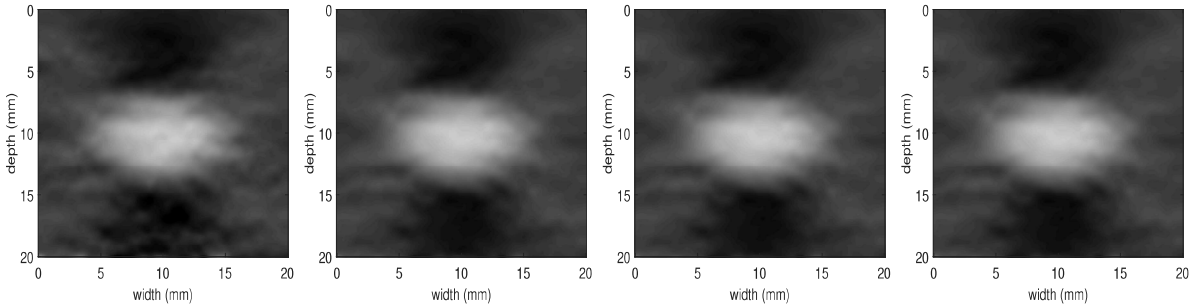

(i) $\alpha_1 = \beta_1 = 5$, $\alpha_2 = \beta_2 = 1$, $\alpha_3 = \beta_3 = 0$ (j) $\alpha_1 = \beta_1 = 5$, $\alpha_2 = \beta_2 = 1$, $\alpha_3 = \beta_3 = 1$ (k) $\alpha_1 = \beta_1 = 5$, $\alpha_2 = \beta_2 = 1$, $\alpha_3 = \beta_3 = 5$ (l) $\alpha_1 = \beta_1 = 5$, $\alpha_2 = \beta_2 = 1$, $\alpha_3 = \beta_3 = 20$

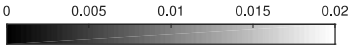

(m) Color bar

Figure A.5: Axial strain images for simulation phantom with different sets of regularization parameter values. Rows 1 shows the axial strain images for different values of α_1 and β_1. Rows 2 represents changes in axial strain images by varying α_2 and β_2. Rows 3 corresponds to the axial strain images for different values of α_3 and β_3. (m) represents the color bar.

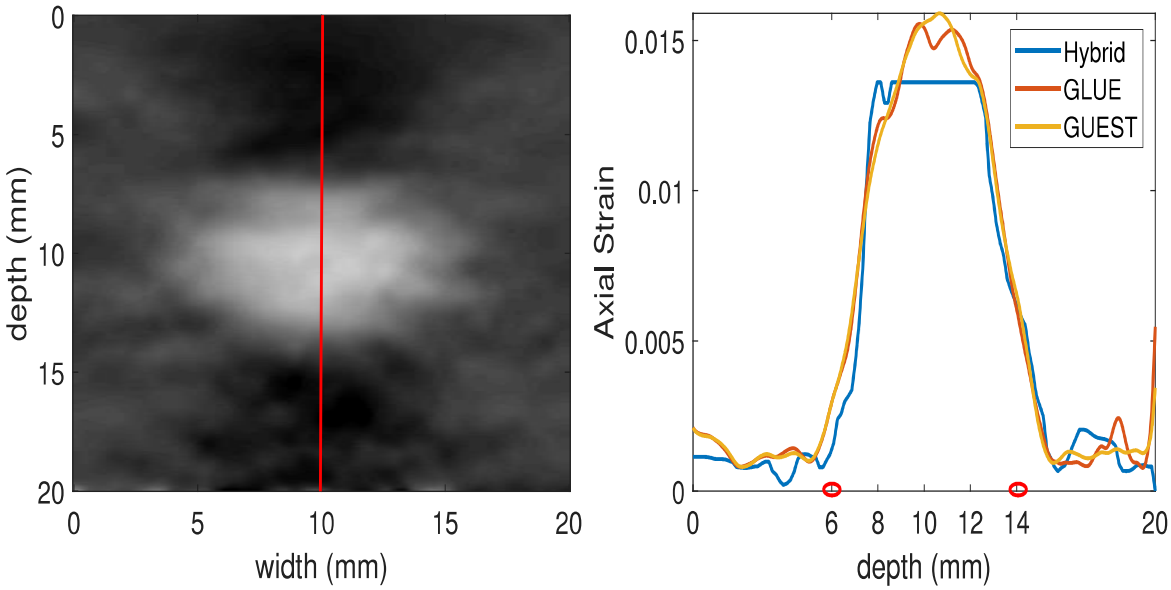

(a) (b)

Figure A.6: One dimensional strain profile. (a) shows the vertical line whose strain is plotted. (b) represents the strain profiles obtained from Hybrid, GLUE and GUEST. Red marked ticks on the horizontal axis represent the beginning and end of the inclusion.

Appendix B

Supplementary Material for RAPID

Figure B.1 shows the schematic description of the set-up for the phantom experiment. Figure B.2 represents the power Doppler images from SVD and RAPID for the simulation data with added random noise of uniform distribution. Two levels of noise with Peak Signal-to-Noise Ratio (PSNR) values of 58.43 dB and 39.34 dB are added to the envelopes of RF data. It is evident from Figure B.2 that the result from SVD for blood rank 15 is similar to that of 19 in case of the lower noise level. On that other hand, the results from SVD for blood subspace ranks 15 and 19 are substantially different from each other for the higher level of noise. This study indicates that the optimal values of tunable parameters of SVD are highly dependent on the noise level. On the contrary, RAPID automatically obtains the optimal result regardless of the level of noise.

Figure B.3 depicts the clutter suppressed power Doppler images for simulation, phantom and *in-vivo* data sets generated by SVD, HOSVD [23] and RAPID. We have incorporated 15 Radio-Frequency (RF) frames to generate the power Doppler images from SVD and RAPID. We consider a data tensor consisting of 3 matrices where each matrix is an ensemble of 15 slow time frames. For SVD and HOSVD, the best results obtained by careful tuning of the parameters are reported. RAPID converges to the optimal results without the need of any manual tuning. The results from SVD and RAPID are very similar to each other. HOSVD does not seem to improve the quality of the power Doppler images for the datasets used in this study. However, HOSVD is expected to improve the result when a large number of data matrices consisting

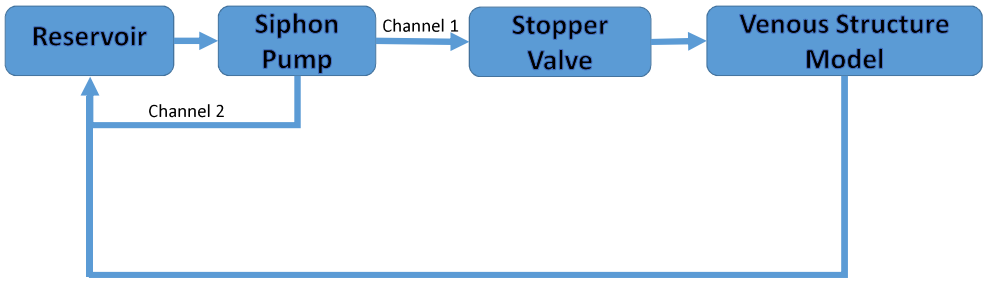

Figure B.1: A schematic depiction of the set-up for the phantom experiment.

of more slow time frames are incorporated to form the data tensor. Therefore, it is suggested that HOSVD improves the result at the expense of extensive amount of data. Besides, this method suffers from much higher running time than SVD and RAPID. To be precise, our MATLAB implementation of HOSVD takes more than 40 minutes to execute for a tensor of 3 matrices each of which consists of 15 slow time frames of size 250×125. On the other hand, both SVD and RAPID take less than 1 second to process the same amount of data. Another limitation of HOSVD is that it has 6 tunable parameters and there is no rigid criterion to select the optimal set of values for them. Hence it is very difficult to obtain the optimal result while dealing with a large dataset since it is subject to the manual tuning of 6 parameters over a certain range. This drawback calls the clinical usefulness of HOSVD into question.

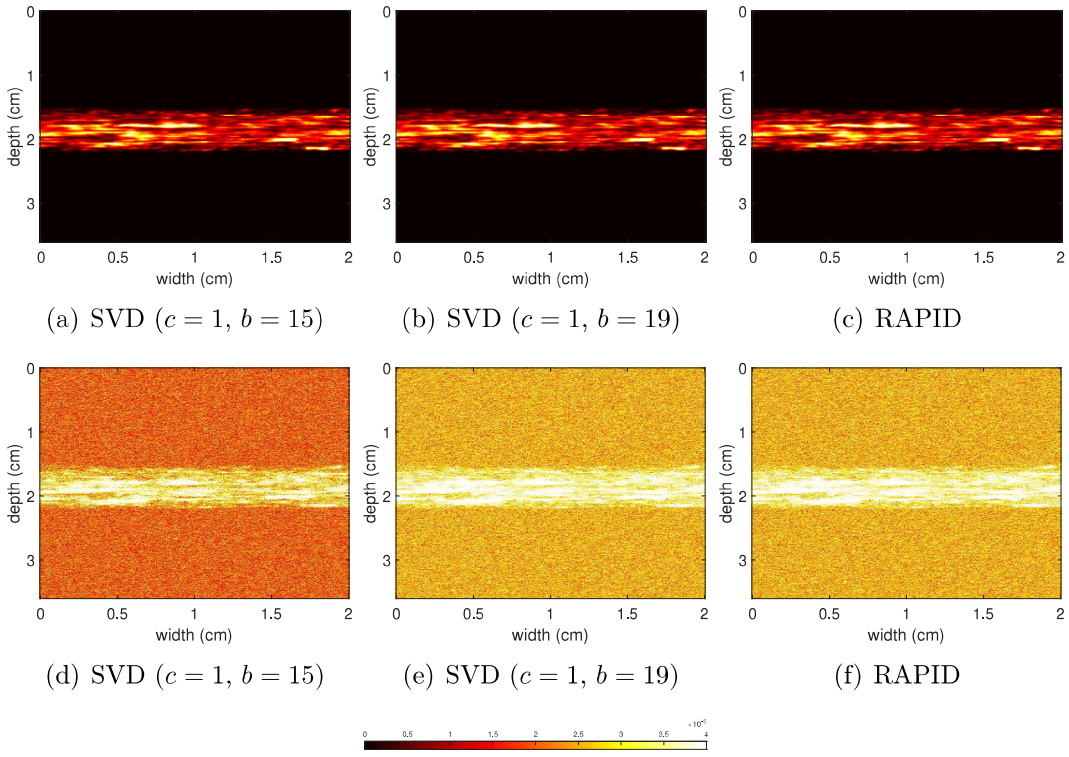

(a) SVD ($c = 1$, $b = 15$) (b) SVD ($c = 1$, $b = 19$) (c) RAPID

(d) SVD ($c = 1$, $b = 15$) (e) SVD ($c = 1$, $b = 19$) (f) RAPID

(g) Color bar

Figure B.2: Power Doppler images for simulation with different noise levels. Rows 1 and 2 correspond to PSNR values of 58.43 dB and 39.34 dB respectively. Columns 1 and 2 show results from SVD for different combinations of subspace ranks. Column 3 represents the results from RAPID. (g) shows the color bar.

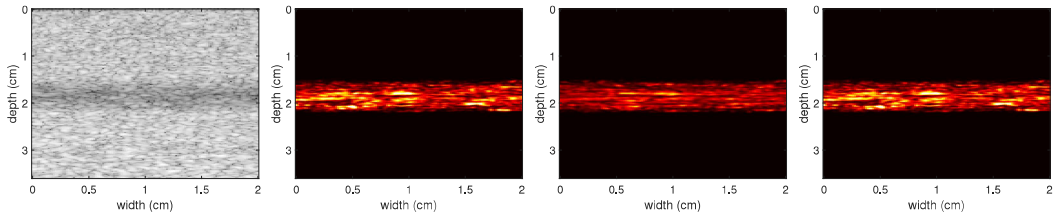

(a) B-mode (b) SVD (c) HOSVD (d) RAPID

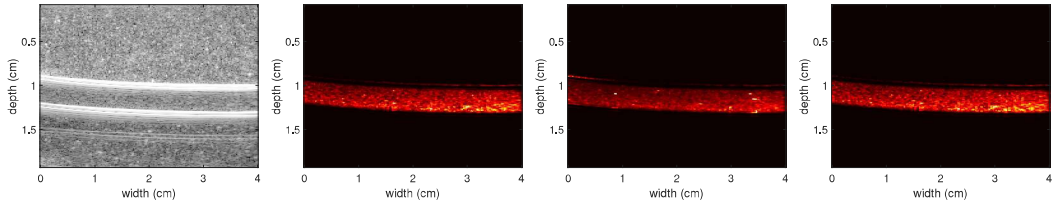

(e) B-mode (f) SVD (g) HOSVD (h) RAPID

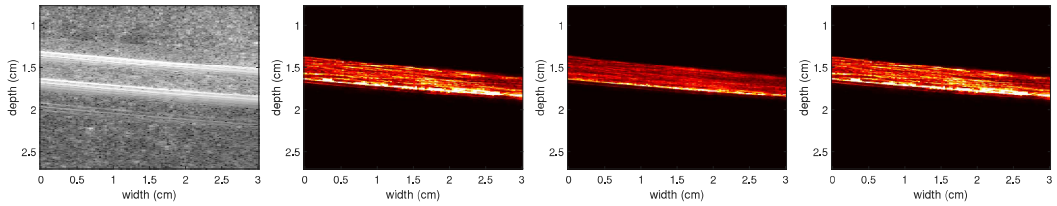

(i) B-mode (j) SVD (k) HOSVD (l) RAPID

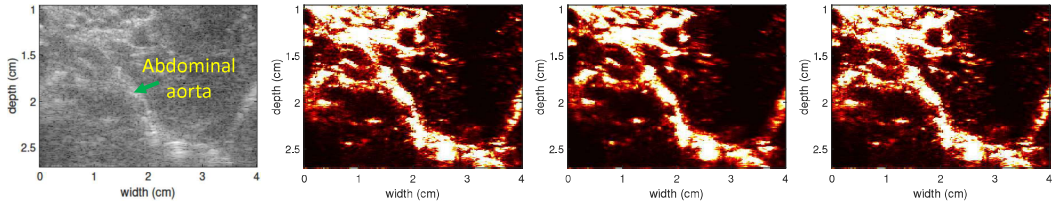

(m) B-mode (n) SVD (o) HOSVD (p) RAPID

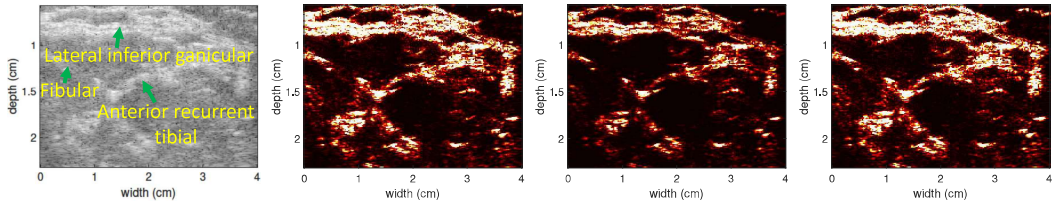

(q) B-mode (r) SVD (s) HOSVD (t) RAPID

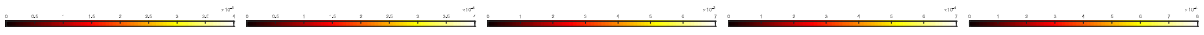

(u) Color bar for simulation results (v) Color bar for focused phantom results (w) Color bar for plane-wave phantom results (x) Color bar for *in-vivo* rat results (y) Color bar for *in-vivo* human knee results

Figure B.3: Power Doppler images for simulation, phantom and *in-vivo* data sets. Rows 1-5 correspond to simulation, phantom with focused imaging, phantom with plane wave imaging, *in-vivo* data from a rat's abdomen and *in-vivo* data from the knee of a human subject respectively. Columns 1-4 depict B-mode, power Doppler images obtained from SVD, HOSVD and RAPID respectively. (u), (v), (w), (x) and (y) represent the color bars.